Studies on structures and functions of EF-hand proteins

January 2014

Nanao Suzuki

Graduate School of Science and Technology

CHIBA UNIVERSITY

Studies on structures and functions of EF-hand proteins

January 2014

Nanao Suzuki

Graduate School of Science and Technology

CHIBA UNIVERSITY

TABLE OF CONTENTS

ABBREVIATIONS4
CHAPTER I
Coordination structures of Mg ²⁺ and Ca ²⁺ in three types of tobacco calmodulins in
solution: Fourier-transform infrared spectroscopic studies of side-chain COO groups
Summary6
1. Introduction
2. Material and Methods12
3. Results
4. Discussion
CHAPTER II
Calcium-dependent structural changes in human reticulocalbin-1
Summary
1. Introduction39
2. Materials and Methods41
3. Results and Discussion

CHAPTER III

Development and evaluation of a new SAXS system for biological samples

Summary	73
1. Introduction	74
2. Development of the system	75
3. Results	77
4. Conclusions	78
ACKNOWLEDGEMENTS	83
REFERENCES	84

ABBREVIATIONS

AEBSF: 4-(2-Aminoethyl) benzenesulfonyl fluoride hydrochloride

ANS: 8-Anilino-1-naphthalenesulfonic acid

ATR: attenuate total reflection

CaM: calmodulin

CD: circular dichroism

CMF: Confocal Max-Flux

EDTA: ethylenediaminetetraacetic acid

EGTA: ethylen glycol bis (β-aminoethylether)-N, N, N', N'-tetraacetic acid

FT-IR: Fourier transform infrared spectroscopy

GI: glucose isomerase

HEPES: 2-[4-(2-hydroxyethyl)-1-piperazine] ethanesulfonic acid

HPLC: high performance liquid chromatography

HR: hypersensitive reaction

hRCN1: human reticulocalbin 1

PDDF: particle distance distribution function

R_g: radius of gyration

SAXS: small angle X-ray scattering

TnC: troponin C

Tris: Tris (hydroxymethyl) aminomethane

TMV: tobacco mosaic virus

CHAPTER I

Coordination structures of Mg²⁺ and Ca²⁺ in three types of tobacco calmodulins in solution: Fourier-transform infrared spectroscopic studies of side-chain COO⁻ groups

Summary

Calmodulin (CaM) is a Ca²⁺-binding protein that regulates a number of fundamental cellular activities. Nicotiana tabacum CaM (NtCaM) comprises 13 genes classified into three types, among which gene expression and target enzyme activation differ. I performed Fourier-transform infrared spectroscopy to compare the secondary and coordination structures of Mg²⁺ and Ca²⁺ among NtCaM1, NtCaM3 and NtCaM13 as representatives of the three types of NtCaMs. Data suggested that NtCaM13 has a different secondary structure due to the weak β-strand bands and the weak 1661 cm⁻¹ band. Coordination structures of Mg²⁺ of NtCaM3 and NtCaM13 were similar but different from that of NtCaM1, while the Ca²⁺-binding manner was similar among the three CaMs. The amplitude differences of the band at 1554-1550 cm⁻¹ obtained by second-derivative spectra indicated that the intensity change of the band of NtCaM13 was smaller in response to [Ca²⁺] increases under low [Ca²⁺] conditions than were those of NtCaM1 and NtCaM3, while the intensity reached the same level under high [Ca²⁺]. Therefore, NtCaM13 has a characteristic secondary structure and specific Mg²⁺-binding manner and needs higher [Ca²⁺] for bidentate Ca²⁺ coordination of 12th Glu in EF-hand motifs. The Ca²⁺-binding mechanisms of the EF-hand motifs of the three CaMs are similar; however, the cation-dependent conformational change in NtCaM13 is unique among the three NtCaMs.

Keywords: Tobacco calmodulin, Infrared Spectroscopy, Secondary structure, Coordination structure

1. Introduction

Calmodulin (CaM) is a multifunctional Ca²⁺-dependent regulator of intracellular processes that associates with and modulates a number of enzymes and ion channels. CaM is found in all eukaryotic cells and its amino acid sequence was strictly conserved during evolution. CaM consists of two globular domains, the N-domain (N-lobe) and the C-domain (C-lobe), which are connected by a highly mobile central region. Each lobe contains two helix-loop-helix EF-hand motifs (GIFFORD *et al.* 2007). This motif contains a Ca²⁺-binding site composed of 12 amino acid residues, where the 1st, 3rd, 5th, 7th, 9th and 12th positions are related to Ca²⁺-ligation. Among these six positions, the 12th Glu residue is conserved within the EF-hand motif and binds Ca²⁺ through a bidentate mode, which plays an important role in Ca²⁺ ligation.

A higher plant species usually possesses several types of CaM isoforms, while a higher animal species has only one type. Furthermore, in plant CaMs, the number of isoforms differs among species. For instance, soybean contains five CaM genes (*SCaM1-5*) encoding four distinct isoforms; namely, SCaM1/3, SCaM2, SCaM4, and SCaM5 (Lee *et al.* 1995), and potato has eight CaM genes (*PCaM1-8*) among which *PCaM2*, *PCaM3* and *PCaM4* were only partially cloned and have not been proven to be functional genes, as well as at least two isoforms, PCaM1, and PCaM5/6/7/8 (TAKEZAWA *et al.* 1995). *Nicotiana tabacum* has 13 CaM genes (*NtCaM1-13*) encoding four isoforms NtCaM1/2, NtCaM3/4/5/6/7/8/11/12, NtCaM9/10 and NtCaM13 (YAMAKAWA *et al.* 2001). These CaM isoforms can be classified into three types based on their amino acid sequence homology (see Fig. I-1). NtCaM1/2 belongs to type I, NtCaM3/4/5/6/7/8/11/12 and NtCaM9/10 differ in only one amino acid and belong to type II, and NtCaM13 belongs to type III. Transcriptional regulation differs among the

three types of NtCaMs. Transcripts of type I NtCaM are accumulated in response to wounding and the tobacco mosaic virus (TMV)-mediated hypersensitive reaction (HR). Type II NtCaM transcripts are constitutively accumulated in leaves and type II isoforms are found predominantly in healthy tobacco leaves (YAMAKAWA *et al.* 2001). Type III NtCaM transcripts are present at low levels in healthy leaves and are dramatically induced by TMV-mediated HR. Type II is a conventional CaM of plants, whereas types I and III are expressed under stress conditions. Type III has the most substituted amino acid sequence compared to the human CaM sequence (Fig. I-1A). NtCaM1, 3 and 13 are representatives of types I, II and III, respectively.

The three types of NtCaMs activate characteristic target enzymes; rat NO synthase is activated most effectively by type III, moderately by type I and weakly by type II (KARITA *et al.* 2004), and plant NAD kinase (NADK) is activated in the inverse order. Calcineurin is activated most highly by NtCaM3 (type II) and moderately activated by NtCaM1 (type I) and 13 (type III) (KARITA *et al.* 2004). Mitogen-activated protein kinase phosphatase shows high affinity to NtCaM1 (type I) and 3 (type II) but lower affinity to NtCaM13 (type III) (YAMAKAWA *et al.* 2004). The Ca²⁺ concentration required for activation also differs among the types; type II activates NADK at Ca²⁺ levels of around 0.1 μM, which corresponds to the cytosolic concentration in unstimulated cells. Type I activates NADK at 1–5 μM, which corresponds to the elevated Ca²⁺ concentration in stimulated cells, while type III does not activate NADK at any Ca²⁺ level. In addition, NtCaM1 (type I) and 3 (type II) activate NADK at cytosolic pH (6.8–7.1) in stimulated cells, while the cytosolic pH of unstimulated cells is ~7.5 (KARITA *et al.* 2004). Thus, type I NtCaMs can activate NADK only in

stimulated cells, while type II NtCaMs can activate NADK in both stimulated and unstimulated cells.

The three-dimensional structures of Ca²⁺-loaded and unloaded animal CaMs, including that of human CaM, have been solved (BABU *et al.* 1985; BABU *et al.* 1988; KUBONIWA *et al.* 1995; ZHANG *et al.* 1995). Three plant CaM structures have been reported; the crystal structure of Ca²⁺-PCaM6 and the solution structures of Ca²⁺-SCaM1 and Ca²⁺-SCaM4 (YuN *et al.* 2004; ISHIDA *et al.* 2008). A calculated structure of the N-terminal domain of Mg²⁺-SCaM4 was also reported (HUANG *et al.* 2010). The solution structures of Ca²⁺-SCaM1, Ca²⁺-SCaM4, and Ca²⁺-animal CaM are highly similar (HUANG *et al.* 2010). SCaM1 exhibits a 90% amino acid sequence identity to animal CaM, but the C-lobe of Ca²⁺-SCaM1 has a more open conformation and consequently a larger hydrophobic target-protein-binding pocket than Ca²⁺-animal CaM or Ca²⁺-SCaM4 (HUANG *et al.* 2010). Thus an amino acid sequence difference of 10% can have a significant effect on the three-dimensional structure.

The three-dimensional structure of NtCaM has not yet been reported. The sequence of NtCaM3 (type II) is 98 and 99% identical to those of PCaM6 and SCaM1, respectively, suggesting that the overall structure of NtCaM3 is similar to those of PCaM6 and SCaM1. The sequence of NtCaM13 (Type III) is 87% identical to that of SCaM4. There is no three-dimensional structure for NtCaM1 orthologs, but NtCaM1 has 92% similarity with SCaM1, and 91% with NtCaM3, PCaM6, and human CaM (CHATTOPADHYAYA *et al.* 1992). NtCaM1 and NtCaM13 may have some similarities in terms of its overall three-dimensional structures and characteristics to SCaM1 and SCaM4, respectively.

I used Fourier-transform infrared spectroscopy (FTIR) to study the secondary structural changes and the coordination structures of Mg²⁺ and Ca²⁺ in NtCaM isoforms. Secondary structure analysis of proteins uses almost exclusively the amide I band. The sensitivity of this band to the structure of the protein backbone is predominantly due to transition dipole coupling. The result is that a particular secondary structure absorbs predominantly in a specific range of the amide I region, typically around 1652 cm⁻¹ for α-helices, around 1630 and 1679 cm⁻¹ for β-sheets, around 1671 cm⁻¹ for turns, and around 1645 cm⁻¹ for disordered structure in D₂O buffer. A broad, featureless amide I band centered near 1650 cm⁻¹ is characteristic of a disordered structure, while aggregated protein often shows a band near or below 1620 cm⁻¹, which is characteristic of intermolecular β-sheets. FTIR is a useful tool for examining protein side chains as well as protein conformations in solution, in combination with resolution-enhancement techniques such as second-derivative and Fourier self-deconvolution methods (ARRONDO et al. 1993; BARTH 2000; BARTH and ZSCHERP 2002; BARTH 2007). A series of FTIR studies combined with these techniques have been performed to investigate the interactions between Ca²⁺ and side chain COO⁻ groups in Ca²⁺-binding proteins, and have shown that the COO stretching vibrational bands can be used to identify the coordination mode of side-chain COO groups (NARA et al. 1994; NARA et al. 1995; NARA et al. 1996; YUMOTO et al. 2001; NARA et al. 2004). The COO groups can coordinate to metal ions in three modes: unidentate, bidentate, and bridging modes. A pseudo-bridging mode is a special case of the bridging mode, where one of the ligands in the bridging coordination is replaced by a water molecule (DEACON and PHILLIPS 1980). The spectral changes in the regions of the COO antisymmetric stretching vibrations are well-correlated with the types of coordination of the COO groups to Ca²⁺

(NARA *et al.* 1994; NARA *et al.* 1995; MIZUGUCHI *et al.* 1997a; MIZUGUCHI *et al.* 1997b; OZAWA *et al.* 2000; NARA and TANOKURA 2008). The antisymmetric stretch of the COO group not coordinated to M²⁺ (M=Mg or Ca) or coordinated to M²⁺ in either the unidentate mode or the pseudo-bridging mode shows a band in the range 1605–1567 cm⁻¹. On the other hand, a shift of COO antisymmetric stretching vibration to a lower wavenumber, around 1552 cm⁻¹, is characteristic of the interaction between a M²⁺ and a COO group in bidentate coordination (NARA *et al.* 1994; NARA *et al.* 1995; NARA *et al.* 1996). Moreover, in the second-derivative spectra of the IR spectra of bovine brain CaM in D₂O buffer, the following bands are known markers of Ca²⁺-bound forms and called marker bands I, II and III, respectively (NARA *et al.* 1995; NARA and TANOKURA 2008): the amide-I' band at about 1662 cm⁻¹, the COO antisymmetric stretching band at about 1553 cm⁻¹, and the COO symmetric stretching band at 1424 cm⁻¹.

In the present study, I measured the FTIR spectra of the three types of NtCaM isoforms to compare the secondary structural changes upon M^{2+} -binding and the interaction of the side-chain COO groups with M^{2+} ions in the Ca^{2+} binding sites. My results show that NtCaM1 has stable α -helices and β -sheets in its structure and that the α -helix and β -sheet structures increase with Mg^{2+} binding, and increase to a greater degree upon Ca^{2+} binding. On the other hand, NtCaM13 has a more disordered structure in M^{2+} -free (apo) form and has fewer β -sheet structures than NtCaM1. In addition, the weak marker band I in NtCaM13 indicated that NtCaM13 had a different secondary structure. With regard to the coordination structures, the Mg^{2+} -binding manner in NtCaM3 and NtCaM13 differed from that in NtCaM1; the 1^{st} , 3^{rd} and 5^{th} Asp side chain COO^- groups of NtCaM3 and NtCaM13 coordinate in pseudo-bridging mode to both Mg^{2+} and Ca^{2+} ions, whereas contribution of the COO^- groups of NtCaM1 to the

coordination may be smaller than those of NtCaM3 and NtCaM13. The 12^{th} Glu side chain COO^- groups coordinate to Ca^{2+} ions in the bidentate mode but do not interact with Mg^{2+} directly in all three types of NtCaMs.

2. Materials and Methods

Expression and Purification

Detailed information regarding construction of the NtCaM1, NtCaM3 and NtCaM13 expression systems has been reported previously (YAMAKAWA et al. 2001). Briefly, cDNAs of NtCaM1, NtCaM3 and NtCaM13 were inserted into pET15b (Novagen). Escherichia coli Rosetta (DE3) (Novagen) was transformed with each of the plasmids and cultivated at 37°C. Protein expression was induced by the addition of 1 mM isopropyl- β -D-thiogalactopyranoside when the culture reached an OD_{600} of 0.6–0.9. After harvesting cells, the cell pellets were suspended in 20 mM Tris-HCl (pH 8.0) containing 10 mM CaCl₂, 0.1 mM 4-(2-aminoethyl) benzenesulfonyl fluoride hydrochloride (AEBSF, Roche), 1 µg/ml E64 and 1 µg/ml leupeptin, then sonicated and clarified by centrifugation. The soluble fraction was heated at 90°C for 5 min, and rapidly cooled on ice. Denatured components were removed as pellets by centrifugation. The supernatant was loaded onto a phenyl-sepharose column (GE healthcare) equilibrated with buffer I (25 mM Tris-HCl (pH 8.0), 5 mM CaCl₂). After washing the column with three column volumes of buffer I, three column volumes of buffer II (25 mM Tris-HCl (pH 8.0), 50 mM NaCl, 1 mM CaCl₂) were applied to the column for more stringent washing. The bound proteins were eluted with buffer III (25 mM Tris-HCl (pH 8.0), 2 mM EGTA). The fractions containing NtCaM were treated with 3% TCA to remove Ca²⁺ and then centrifuged at 5000 rpm for 10 min at 4°C. The precipitate was dissolved in 1 M Tris-HCl (pH8.0) and dialyzed at 4°C against 10 mM Tris-HCl (pH 8.0), 1 mM EDTA and 200 mM NaCl. The dialysate was passed through a Superdex 75 gel-filtration column (GE healthcare). Collected fractions were concentrated, dialyzed at 4°C against water and lyophilized. Using this procedure, I obtained homogeneously purified apo NtCaM.

FTIR measurements

To obtain reliable IR spectra in the regions of the COO antisymmetric stretch and the amide-I' band, exchangeable protons in the apo NtCaM proteins were completely deuterated by incubation in D₂O at 60°C, as described previously (YUMOTO et al. 2001). Apo, Mg²⁺-bound and Ca²⁺-bound NtCaM proteins for FTIR measurements were obtained by dissolving the lyophilized powder of the deuterated apo protein in D₂O/H₂O buffer (20 mM HEPES-NaOH/D (pH 7.4 / pD 7.6), 100 mM NaCl) containing non-metal cations, 100 mM MgCl₂, and 100 mM CaCl₂, respectively. Proteins for Ca²⁺ titration experiments were also obtained in D₂O buffer containing 20 mM HEPES-NaOD (pD 7.8), 100 mM NaCl, 4 mM MgCl₂, and X mM CaCl₂ (X = 0, 0.5, 1, 1.5, 2, 3, 4, 6, 8, 10, 12, 20). The protein concentrations for the FTIR measurements were adjusted to 2.0 mM. FTIR spectra were measured at room temperature on a PerkinElmer Spectrum One Fourier-transform infrared spectrometer. ATR-FTIR measurements were carried out for the divalent cation difference measurements of NtCaMs at room temperature on the infrared spectrometer equipped with an ATR unit and an MCT detector at 2 cm⁻¹ resolution. Approximately 0.010 ml of a sample solution was placed on a Diamond/ZnSe 1-reflection top-plate (Perkin-Elmer) (NARA et al. 2008; NARA et al. 2013). FTIR measurement for Ca²⁺ titration experiments were carried out on the infrared spectrometer equipped with a TGS detector, at 2 cm⁻¹ resolution.

Sample solution (0.012 ml) was placed between two BaF₂ plates separated by a 0.012-mm thick mylar spacer. The gap between the two BaF₂ plates was sealed with aluminum tape to prevent water evaporation. For all measurements, interferograms from 200 scans were averaged to obtain one spectrum. Nitrogen gas was constantly pumped into the spectrometer to eliminate water vapor. The IR spectra of solvent for each sample were measured using the same method. I confirmed in advance that an ATR-FTIR spectrum for NtCaM gives the same results as the FTIR spectra in the region of 1800-1300 cm⁻¹.

Data analyses for FTIR spectra

To eliminate the contribution of H_2O/D_2O , the spectrum of solvent alone was subtracted from that of the protein solution after multiplying by an appropriate factor. Second derivative and difference spectra were calculated using IGOR PRO 3.21 (WaveMetrics. Lake Oswego. USA). The amplitude difference between Ca^{2+}/Mg^{2+} -bound and apo forms was calculated using the second derivative band at 1515 cm⁻¹ (CC stretching mode of the tyrosine ring) as an internal standard since this band is not related to Ca^{2+} or Mg^{2+} binding.

3. Results

Comparison of amino acid sequences among animal and plant CaMs

Figure I-1A shows the amino acid sequences of seven plant CaMs—classified into three types—and two vertebrate CaMs. All CaMs have four EF-hand motifs (Fig. I-1A, asterisks). Amino acid variations specific to all the plant CaMs compared to the animal CaMs are found at the 27th, 71st (except SCaM4), 72nd, 86th, 87th and 97th

residues (Fig. I-1A, gray colored). Type III isoforms have more variations throughout their sequences than type I and type II isoforms (Fig. I-1A).

FTIR spectra for apo, Mg^{2+} -bound and Ca^{2+} -bound NtCaMs

I performed FTIR measurements of M^{2+} -bound and apo NtCaM1, NtCaM3 and NtCaM13 in D_2O and H_2O buffers (Figs. I-2 and I-3). Figure I-2 shows attenuate total reflection (ATR)-IR absorbance spectra and Figure I-3 shows the corresponding second-derivative spectra. In these two figures, panels A, B and C show the spectra of NtCaM1, NtCaM3 and NtCaM13, respectively. In each panel, the spectra of (a), (b) and (c) were measured in D_2O buffer and (d), (e) and (f) in H_2O buffer. (a) and (d) are the spectra of the apo form, (b) and (e) of the Mg^{2+} -bound form, and (c) and (f) of the Ca^{2+} -bound form.

IR spectra of NtCaM1, NtCaM3 and NtCaM13

Four common bands were observed among the three types of NtCaMs in D₂O buffer (Fig. I-2A-C, (a)-(c)); the amide-I' band at 1646-1642 cm⁻¹, the COO antisymmetric stretching band at 1597–1571 cm⁻¹, the amide-II' band at 1454–1442 cm⁻¹, and the COO symmetric stretching band at 1406–1402 cm⁻¹. Four bands were identified in H₂O buffer (Fig. I-2A–C, (d)-(f)): the amide I band at 1650–1647 cm⁻¹, the amide II band at 1549–1547 cm⁻¹, the CH₂ bending band at around 1455 cm⁻¹, and the COO symmetric stretching band at 1405–1401 cm⁻¹. These main bands seemed to be similar among the apo, Mg²⁺-bound and Ca²⁺-bound forms of each NtCaM in both D₂O and H₂O buffers. However, three clear differences were observed in the COO antisymmetric stretch region (1620–1530 cm⁻¹); (1) In Mg²⁺-bound form in D₂O buffer, the bands at 1597 cm⁻¹ of NtCaM3 and 1583 cm⁻¹ of NtCaM13 were broader than the

corresponding NtCaM1 bands. (2) In D₂O solution, the bands at 1584–1577 cm⁻¹ in the Ca²⁺-bound forms of all three types of NtCaMs (Fig. I-2A–C, (c)) were shifted higher than the corresponding bands of apo forms (Fig. I-2A–C, (a)) and there appeared a shoulder on the band which was not observed on the corresponding bands of the apo and Mg²⁺-bound forms. In addition, the bands at 1582 and 1584 cm⁻¹ of Ca²⁺-bound NtCaM3 and NtCaM13, respectively, were sharp compared with the corresponding bands of NtCaM1. (3) In H₂O buffer, the bands around 1590 cm⁻¹ of NtCaM3 and those at 1590–1581 cm⁻¹ of NtCaM13 were observed in the spectra of M²⁺-bound forms but not in the spectra of NtCaM1. Differences among the spectra become clear in the second-derivative spectra, as described below.

Second-derivative spectra of three types of NtCaM isoforms

Figure I-3 shows the second-derivative spectra of the corresponding spectra in Figure I-2. In these spectra, two types of bands were observed: 1) Bands related to the secondary structure of the protein in the amide I' region (1700–1620 cm⁻¹) and 2) bands related to the coordination state in the COO⁻ antisymmetric stretch region (1620–1530 cm⁻¹) and in the COO⁻ symmetric stretching region (1430–1370 cm⁻¹).

1. Secondary structural change

In the amide-I' region of the three types of NtCaMs (Fig. I-3A–C), two common bands were observed at 1677–1674 and 1648–1642 cm⁻¹ in the apo, Mg^{2+} -bound and Ca^{2+} -bound forms (Fig. I-3A–C, (a)–(c)). In addition, all bands around 1648–1642 cm⁻¹ in D_2O buffer had shoulders or small peaks at around 1631 cm⁻¹. The weak common bands at 1677–1674 cm⁻¹ and the shoulder bands at around 1631 cm⁻¹ in D_2O buffer were assigned to β -sheet structures (FABIAN *et al.* 1996; BARTH 2000;

BARTH 2007) and corresponding bands were observed at 1683–1681 cm⁻¹ and at around 1631 cm⁻¹ in H₂O buffer. The strongest bands at 1648–1642 cm⁻¹ in D₂O buffer and at 1651–1649 cm⁻¹ in H₂O buffer were related to the CaM secondary structure, mainly the helix structure (FABIAN et al. 1996; BARTH 2000; BARTH 2007). In this region, three differences were observed; (1) characteristic bands at 1662 cm⁻¹ were observed in the Ca²⁺-bound form in NtCaM1 and NtCaM3 (Fig. I-3A-B, (c)), as well as bovine brain CaM (NARA et al. 1995), but not in NtCaM13 (Fig. I-3C, (c)). This 1662 cm⁻¹ band in the Ca²⁺-bound form is thought to be associated with the secondary structure of the protein main chain (NARA and TANOKURA 2008) and was classified as marker band I, which is considered to be characteristic of the active type (NARA et al. 1995). (2) The strongest bands at 1647-1642 cm⁻¹ in the apo form were broader than that in the M²⁺-bound form of all three types of NtCaMs, which suggested that the structure of the apo form is disordered (BARTH 2007). (3) The bands or shoulders at around 1631 cm⁻¹ appeared in NtCaM1, weakly in NtCaM3, and slightly in NtCaM13. The intensity also increased with M^{2+} binding and had the order: Ca^{2+} -bound > Mg^{2+} -bound > apo form. These differences might be associated with the β -sheet structural intensity.

2. The coordination structures

NtCaM1: In the COO⁻ antisymmetric stretch region, three bands were observed in the apo, Mg²⁺-bound, and Ca²⁺-bound forms of NtCaM1 (Fig. I-3A, (a)–(c)). Those at 1606–1603 cm⁻¹ showed only a slight shift among the apo, Mg²⁺-bound and Ca²⁺-bound forms and may be due to side-chain COO⁻ groups (YUMOTO *et al.* 2001). The bands at 1582 and 1565 cm⁻¹ in the apo form are due to the side-chain COO⁻ groups of Asp and Glu, respectively (NARA *et al.* 1994). The band at 1582 cm⁻¹ in the apo form also showed a 2 cm⁻¹ higher shift in the Mg²⁺-bound form and 3 cm⁻¹ lower shift in the

Ca²⁺-bound form compared with the corresponding band in the apo form. The band at 1584 cm⁻¹ in Mg²⁺-bound NtCaM1 (Fig. I-3A, (b)) had a higher intensity than the 1582 cm⁻¹ band in the apo form and was similar to that in Mg²⁺-bound bovine brain CaM (NARA *et al.* 1995). This increasing amplitude of the 1584 cm⁻¹ band in Mg²⁺-bound NtCaM1 indicates that the 1st, 3rd and 5th Asp may coordinate Mg²⁺ in the pseudo-bridging mode. The amplitude of the band at 1579 cm⁻¹ in the Ca²⁺-bound form was notably stronger than those in the apo and Mg²⁺-bound forms. The 1579 cm⁻¹ band is due to the 1st, 3rd and 5th Asp residues bound to Ca²⁺ in pseudo-bridging mode. The specific band at 1552 cm⁻¹ in the Ca²⁺-bound form showed 13 and 11 cm⁻¹ downshifts from the 1565 and 1563 cm⁻¹ bands in the apo and Mg²⁺-bound forms, respectively, due to the COO⁻ groups of the 12th Glu in EF-hand motifs coordinated to Ca²⁺ in bidentate mode. This band was classified as marker band II of the active form (NARA *et al.* 1995).

In the COO⁻ symmetric stretching region, weak bands at 1425–1423 cm⁻¹ appeared in D₂O buffer, and corresponding bands were seen at 1426–1422 cm⁻¹ in H₂O buffer. The amplitudes of these bands were in the order; Ca²⁺-bound > Mg²⁺-bound > apo form, and this difference was seen more clearly in the spectra taken in H₂O buffer (Fig. I-3A, (d)–(f)). This 1425 cm⁻¹ band was characterized as marker band III, and was thought to be associated with the interaction between M²⁺ and COO⁻ groups in the side chains of Asp and Glu residues (NARA *et al.* 1995; NARA and TANOKURA 2008). Strong bands at 1402 cm⁻¹ were also observed in D₂O buffer, and were thought to be due to the symmetric stretch of the COO⁻ groups of both Asp and Glu residues not coordinated to M²⁺ (NARA *et al.* 1995). The characteristics of most of the bands of NtCaM1 were very similar to those of the corresponding bands of bovine brain CaM (NARA *et al.* 1995).

NtCaM3 and NtCaM13: The main bands were similar to those of NtCaM1 in the COO antisymmetric and symmetric stretch regions. However, compared to NtCaM1, there were three differences in COO antisymmetric stretching region; (1) there was no band at around 1605 cm⁻¹ in the apo form of NtCaM13 (Fig. I-3C, (a)) although there was a corresponding band at 1610 cm⁻¹ in the Ca²⁺-bound form (Fig. I-3C, (c)), indicating that there are some differences in the side-chain COO groups of apo NtCaM13. (2) Characteristic bands at 1601-1600 cm⁻¹ were observed in the Mg²⁺-bound forms of NtCaM3 and NtCaM13 (Fig. I-3B-C, (b)). These bands had a resemblance to those in the Mg²⁺-bound form of Akazara scallop troponin C (TnC) which were characterized as the 1st and 3rd Asp residues in the 4th EF-hand site bound to Mg²⁺ in the pseudo-bridging coordination mode (YUMOTO et al. 2001; NARA and TANOKURA 2008). (3) The bands at 1584 and 1554 cm⁻¹ in the Ca²⁺-bound form of NtCaM13 were stronger than those in NtCaM1 and NtCaM3. In addition, there were two differences in the COO symmetric stretching region; (1) marker band III showed lower shifts in the Ca²⁺-bound form of NtCaM13 in both D₂O and H₂O buffers (Fig. I-3C, (c) and (f)), and (2) the amplitude of the band at 1404–1402 cm⁻¹ decreased with M²⁺ binding in NtCaM3 and NtCaM13 and had the order; apo > Mg²⁺-bound > Ca²⁺-bound forms. The spectra of NtCaM3 and NtCaM13 were similar to each other.

The amplitude-difference spectra of three types of NtCaM isoforms

Figure I-4 shows the amplitude-difference spectra of NtCaM isoforms between the second-derivative spectra of M²⁺-bound forms and those of the apo forms. Most of the bands corresponded with the second-derivative spectra (Fig. I-3). In the amide-I' region, positive common bands were observed at 1678–1676, 1649–1644 and 1630–1629 cm⁻¹

in the Mg²⁺-bound forms and at 1676-1674, 1663-1661 and 1645-1643 cm⁻¹ in the Ca²⁺-bound forms of all three types of NtCaMs. The 1649–1643 cm⁻¹ bands corresponded to helix structures and the other two weak bands at 1678-1675 and 1631–1629 cm⁻¹ to β-sheet structures. In association with the helix structure, the 1649 cm⁻¹ band in the Mg²⁺-bound form of NtCaM13 showed clear shifts compared to the corresponding bands of NtCaM1 and NtCaM3, indicating that the Mg2+-bound form of NtCaM13 has different secondary structure characteristics. In addition, the intensities of 1649-1643 cm⁻¹ bands had the order; NtCaM13 > NtCaM1 > NtCaM3 in the Mg²⁺-bound forms and NtCaM1 > NtCaM3 > NtCaM13 in the Ca²⁺-bound forms. Excluding the band at 1649 cm⁻¹ in the Mg²⁺-bound form of NtCaM13, the amplitude orders of the Mg²⁺-bound and Ca²⁺-bound forms were identical, which indicates that the effects of M2+ binding on conformational changes differ among the three types of NtCaMs. In association with the β-sheet structure, the 1631–1629 cm⁻¹ band appeared strongly in NtCaM1, weakly in NtCaM3, and slightly in NtCaM13, which was identical to what was observed in the second-derivative spectra. Moreover, the band intensities of the Ca²⁺-bound forms were stronger than those in Mg²⁺-bound forms of all three types of NtCaMs. These results indicate that β-sheet structures may contribute more to the Ca²⁺-bound form than to the Mg²⁺-bound form and also contribute the most to the structure of NtCaM1 and the least to that of NtCaM13 among the three types. Furthermore, the 1663–1661 cm⁻¹ band (marker band I) appeared in the difference spectra of NtCaM13 but not in the second-derivative spectra (Fig. I-3C, (c)). This result indicates that NtCaM13 has marker band I, similar to NtCaM1 and NtCaM3, but that it was obscured by the other spectrum.

In association with coordination structures, the characteristic bands at 1601 cm⁻¹ were evident in NtCaM3 and NtCaM13 in the Mg²⁺-bound forms but not in NtCaM1, which instead exhibited a band at 1586 cm⁻¹ in the COO⁻ antisymmetric stretching region. In the Ca²⁺-bound form, the positive common bands appeared at 1610–1600, 1586–1579 and 1554–1550 cm⁻¹. These bands corresponded to those observed in the second-derivative spectra (Fig. I-3A–C, (b)–(c)). The bands at 1586–1579 cm⁻¹ in the Ca²⁺-bound forms were due to the 1st, 3rd and 5th Asp residues bound to Ca²⁺ in pseudo-bridging mode, and the bands at 1554–1550 cm⁻¹ in the Ca²⁺-bound forms were due to the 12th Glu in EF-hand motifs bound to Ca²⁺ in bidentate mode. In the COO⁻ symmetric stretching region, two positive bands at 1426–1417 cm⁻¹ (marker band III) and 1406–1403 cm⁻¹ appeared in all three types of M²⁺-bound NtCaMs with the exception that the Ca²⁺-bound form of NtCaM13 did not show positive band at 1406-1403 cm⁻¹. Marker band III showed downshifts to 1419 and 1417 cm⁻¹ in the Ca²⁺-bound forms of NtCaM3 and NtCaM13, respectively.

Ca²⁺-titration experiments with FTIR

Figure I-5 shows the Ca²⁺-dependent amplitude plots of marker bands I and II. The amplitude-difference spectra were obtained by subtracting the second-derivative spectra data of 0 mM Ca²⁺ from each of 0.5–20 mM Ca²⁺ using the band at 1515 cm⁻¹ as an internal standard. Figure I-5A shows the Ca²⁺-dependent amplitude plots of marker band I derived from the second-derivative spectra. The amplitude of marker band I increased gradually with increasing Ca²⁺ concentrations in all three types of NtCaMs. Marker band I of NtCaM13 was not strongly visible in the second derivative spectrum (Fig. I-3C, (c)), but was present in the difference spectra (Figs. I-4C, (c) and I-5A). The amplitude of marker band I in NtCaM13 was weaker than those in NtCaM1 and

NtCaM3, even at the higher Ca^{2+} concentration. The maximum amplitude at 20 mM Ca^{2+} was ~60% of those of NtCaM1 and NtCaM3.

Marker band II was also Ca²⁺-dependent, and reflected the side-chain COO group of Glu bound to Ca²⁺ in the bidentate coordination. The amplitude of NtCaM13 was weaker than those of NtCaM1 and NtCaM3 at low Ca²⁺ concentrations, while the amplitude of marker band II in NtCaM13 plateaued at the same level as those in NtCaM1 and NtCaM3 at high Ca²⁺ concentrations (Fig. I-5B).

4. Discussion

In contrast to the mammalian system, in which a single CaM isoform operates, plants have multiple types of CaM isoforms, each of which has different functions in transduction of Ca²⁺ signals. NtCaM has four isoforms that are classified into three plant-specific types. NtCaM1, NtCaM3 and NtCaM13 are representatives of types I, II and III, respectively. Although NtCaMs have very high amino acid sequence homologies with animal CaM, the various types have different Ca²⁺ sensitivities and functions in the physiological environment (YAMAKAWA *et al.* 2001; KARITA *et al.* 2004). My interest in the present study was focused on the coordination structures of Mg²⁺ and Ca²⁺ in the Ca²⁺-binding site as well as the protein conformation. I analyzed the physicochemical properties of these three types of plant NtCaM isoforms using IR spectroscopy.

NtCaM1 showed spectra identical to those of bovine brain CaM (NARA *et al.* 1995) in all apo, Mg²⁺-bound, and Ca²⁺-bound forms, suggesting that NtCaM1 binds Mg²⁺ and Ca²⁺ ions in the same manner as bovine brain CaM. Compared with NtCaM1,

both NtCaM3 and NtCaM13 showed similar spectra in the apo forms but not in the Mg²⁺-bound forms. The bands at 1601–1600 cm⁻¹, which were observed in Akazara scallop TnC (YUMOTO *et al.* 2001), were evident in the Mg²⁺-bound forms of both NtCaM3 and NtCaM13 but not NtCaM1. In terms of the Ca²⁺-bound form, NtCaM3 was similar to NtCaM1; NtCaM13 also showed similar main peaks, with the exception of the weak marker band I.

The amplitude plots of marker bands I and II in NtCaM13 (Fig. I-5) indicated different Ca²⁺ sensitivities. For marker band I, the amplitude of NtCaM13 was lower than those of NtCaM1 and NtCaM3, and the maximum amplitude was 60%, even at the high Ca²⁺ concentration. In contrast, for marker band II, the maximum amplitude of NtCaM13 was identical to the other two forms at high Ca²⁺ concentrations, but was lower at low Ca²⁺ concentrations. Marker band I is thought to be associated with the secondary structure of the protein main chain (NARA *et al.* 1995; NARA and TANOKURA 2008). In addition, marker band II is due to the COO groups of the 12th Glu in EF-hand sites coordinated to Ca²⁺ in bidentate mode. The results in Fig. I-5 are indicative of the following two specific characteristics of NtCaM13.

- 1. The results of marker band I indicate that the secondary structure of NtCaM13 differs from those of NtCaM1 and NtCaM3, and that NtCaM13 might have a partially unfolded structure compared to NtCaM1 and NtCaM3, due to the 60% maximum amplitude level.
- 2. Based on marker band II, all four EF-hand motifs of NtCaM13 could bind Ca²⁺ in bidentate mode because the maximum intensity of NtCaM13 was identical to those of NtCaM1 and NtCaM3. However, the binding of 12th Glu residues of NtCaM13 to Ca²⁺ in bidentate mode required higher [Ca²⁺] than those of NtCaM1 and NtCaM3.

The reason for this result is to be clarified, but transition from close to open conformation of NtCaM13might need higher [Ca²⁺] than NtCaM1 and NtCaM3, since it is known that Ca²⁺ binding to CaM induces a transition from close to open conformation (ZHANG *et al.* 1995) and the bidentate coordination of 12th Glu residues in EF-hand motifs is related to the open conformation (GRABAREK 2005). Differences in the local environment in each of the EF-hand sites between NtCaM13 and the other NtCaMs should be also considered.

Secondary structural changes of NtCaM1, NtCaM3 and NtCaM13

The amide I band of proteins is sensitive to secondary structure. In this region, I found differences among the three types of NtCaM isoforms associated with α -helix structures, β -sheet structures, and marker band I.

In previous studies, bands at around 1652 cm⁻¹ were assigned to α-helices and that at 1645 cm⁻¹ to a disordered structure (BARTH 2007; KONG and YU 2007). The amide-I' bands of three types of NtCaMs were observed at 1649–1642 cm⁻¹ (Fig. I-4A–C). These were assigned to the α-helix structure, since the corresponding bands at 1645–1642 cm⁻¹ for bovine brain CaM were assigned to α-helix (NARA *et al.* 1995; BARTH 2007). The amplitude of the amide-I' band increased upon M²⁺ binding and had the order: Ca²⁺-bound > Mg²⁺-bound forms for NtCaM1 and NtCaM3. This is consistent with reports that CaM is an α-helix rich protein (BABU *et al.* 1985), and that its helix content increases upon binding of metal ions (BAYLEY and MARTIN 1992). In contrast, for NtCaM13, the band at 1645 cm⁻¹ in the Ca²⁺-bound form was weaker than the 1649 cm⁻¹ band in the Mg²⁺-bound form (Fig. I-4C). The apo form of NtCaM13 may have a partially unfolded structure compared to NtCaM1 and NtCaM3, and the overlapping

positions of the α -helix and disordered structure bands may have resulted in the reduced intensity of the band at 1645 cm⁻¹ of Ca²⁺-bound NtCaM13. The 1649 cm⁻¹ band of Mg^{2+} -bound NtCaM13 (Fig. I-4C, (a)) was shifted closer to the average α -helix band at 1652 cm⁻¹. This may be due to the fact that Mg²⁺-bound NtCaM13 has fewer water-exposed α -helix structures since the water exposed α -helix band showed a lower shift. The 1649 cm⁻¹ band was higher than both the 1645 cm⁻¹ band of Ca²⁺-bound NtCaM13 and those of Mg²⁺-bound forms of NtCaM1 and NtCaM3 (Fig. I-4C). This indicates that Mg²⁺ binding increases the α-helix structures in NtCaM13. Thus, Mg²⁺ binding is vital for maintenance of proper folding of NtCaM13. SCaM4 has an unfolded conformation in its N-terminal domain and folded conformation in its C-terminal domain in the apo form, but binding of Mg²⁺ to the EF-hand in the N-terminal domain converts the unfolded lobe to a well-folded conformation (HUANG et al. 2010). NtCaM13 has an 87% similar amino acid sequence and is classified as the same type as SCaM4. Thus, NtCaM13 may undergo similar conformational changes upon Mg²⁺-binding as SCaM4. These structural differences between NtCaM13 and NtCaM1 and NtCaM3 may be associated with the low Ca²⁺ affinity.

In the general CaM structure, the β -strand is located in the loop of EF-hand motifs, and the EF-hand is stabilized by the antiparallel β -sheet structure. This antiparallel β -sheet connecting the Ca²⁺-binding loops may play an important role in Ca²⁺-binding and in Ca²⁺-induced conformational changes (GRABAREK 2005; GRABAREK 2006; SENGUEN and GRABAREK 2012). Weak peaks around 1675 cm⁻¹ and shoulders or small bands around 1630 cm⁻¹ were observed in both the second-derivative spectra (Fig. I-3) and the amplitude-difference spectra (Fig. I-4). These bands are assigned to antiparallel β -sheets (BARTH 2007) and were marked in the Mg²⁺-bound and

Ca²⁺-bound forms of NtCaM1, weak in NtCaM3 and slight in NtCaM13. The amplitude of the 1633–1631 cm⁻¹ bands had the order; apo < Mg²⁺-bound < Ca²⁺-bound form in NtCaM1 (Fig. I-3A); an identical tendency is shown in Fig. I-4A. The corresponding bands in H₂O buffer were observed at around 1681 and 1631 cm⁻¹. These bands showed the same characteristics as those in D₂O buffer. My data are suggestive of differences in stabilization by the β-sheet structures among the three types of NtCaM isoforms in solution. NtCaM isoforms increase their β-sheet structures upon M²⁺ binding, and Ca²⁺ binding induces greater stabilization than does Mg²⁺ binding. However, among the three types of NtCaM isoforms, NtCaM1 may be more stabilized by the β-sheet structure than NtCaM3 or NtCaM13, while NtCaM13 has an unstable structure with fewer β-sheet structures.

Marker band I is thought to be associated with the secondary structure of the protein main chain (NARA and TANOKURA 2008). Marker band I is observed in the spectra of CaM (TREWHELLA *et al.* 1989; NARA *et al.* 1995; FABIAN *et al.* 1996) and Turkey TnC (BERRIDGE *et al.* 1998), but not in Akazara scallop TnC (YUMOTO *et al.* 2001) or parvalbumin (JACKSON *et al.* 1991) (Table I-1). For CaM, full-length CaM and each domain show marker band I (TREWHELLA *et al.* 1989; NARA *et al.* 1995; FABIAN *et al.* 1996), indicating that marker band I is not related to the central helix structure of CaM. The most obvious difference between CaM/Turky TnC and parvalbumin/Akazara scallop TnC is the number of Ca²⁺-binding active EF-hand motifs. CaM and Turky TnC have four EF-hand motifs; however, parvalbumin has only two and Akazara scallop TnC has only one active EF-hand among the four motifs. Thus, the lower number of active EF-hand sites may induce less secondary structure change. For NtCaM, marker band I was clearly visible in the spectra of both NtCaM1 and NtCaM3, but only weakly

in NtCaM13, indicating that the secondary structure of NtCaM13 changed upon Ca²⁺ binding. However, the structure of NtCaM13 may contain partially unfolded domains compared to NtCaM1 and NtCaM13.

The coordination structure of NtCaM1, NtCaM3 and NtCaM13

The Ca²⁺ binding sites of the three types of NtCaMs are shown in Figure I-1B. Applying the general rule of EF-hand motifs to these proteins, the COO groups of the 1st, 3rd and 5th Asp and 12th Glu should coordinate to Ca²⁺ directly. Based on the crystal structure of vertebrate CaMs (BABU *et al.* 1988), the COO groups of Glu at the 12th position in four EF-hand sites may bind to Ca²⁺ ions in the bidentate coordination mode, and the COO groups of Asp at the 1st, 3rd and 5th positions may bind to Ca²⁺ in the unidentate coordination mode. I interpreted the bands in the COO antisymmetric stretching region for NtCaMs in relation to the coordination structures of the COO groups and the peak positions of the COO stretching bands mentioned above.

- (a) The bands at 1601 cm⁻¹ of Mg²⁺-bound NtCaM3 and NtCaM13 in Fig. I-4 indicate that the COO⁻ groups of the 1st, 3rd and 5th Asp interact with Mg²⁺ in pseudo-bridging mode; this band was not observed in NtCaM1.
- (b) The band at 1584 cm⁻¹ of Mg²⁺-bound NtCaM1 (Fig. I-3A, (b)) had a higher amplitude than the 1582 cm⁻¹ band in the apo form, suggesting the contribution of 1st, 3rd, and 5th Asp to Mg²⁺-coordination in pseudo-bridging mode, but the contribution may be smaller than those of the Asp residues of NtCaM3 and NtCaM13. Alternatively, the Asp residues of NtCaM1 may not interact with Mg²⁺ directly.

- (c) The band at 1554–1551 cm⁻¹ known as marker band II, was observed in all Ca²⁺-bound forms. Therefore, the COO⁻ groups of the 12th Glu residues bind to Ca²⁺ in bidentate coordination mode in all three types of NtCaMs.
- (d) The amplitude of marker band II of NtCaM13 was low at low Ca²⁺ concentrations (Fig. I-5B) compared to NtCaM1 and NtCaM3, indicating that the 12th Glu residues of NtCaM13 require a higher [Ca²⁺] than those of NtCaM1 and NtCaM3 to fully bind Ca²⁺ in bidentate coordination mode in all EF-hand sites.
- (e) The bands at 1584–1579 cm⁻¹ appeared in the Ca²⁺-bound forms of all three types, indicating that the COO groups of the 1st, 3rd and 5th Asp residues interact with Ca²⁺ in pseudo-bridging mode.

As a result, I propose the Mg^{2+} and Ca^{2+} coordination models for NtCaM3, the representative NtCaM, as shown in Fig. I-6. 1^{st} , 3^{rd} and 5^{th} Asp residues bind to Mg^{2+} in pseudo-bridging mode but 12^{th} Glu residues do not bind Mg^{2+} , while both Asp and Glu residues in EF-hand sites bind Ca^{2+} in pseudo-bridging mode and bidentate mode, respectively.

Intracellular free Ca²⁺ concentrations fluctuate between 10⁻⁷ M at rest and 10⁻⁵ M during activation (BERRIDGE *et al.* 1998; BERRIDGE *et al.* 2000). In contrast, free Mg²⁺ levels are relatively constant within the range 0.5–1.0 mM in most cells (ROMANI 2011). Also, NtCaMs might bind Mg²⁺ in resting cells. Based on this hypothesis, the Mg²⁺-bound form is likely the initial form in resting cells, and Ca²⁺-binding occurs in the presence of a large excess of Mg²⁺. Differences in the Mg²⁺ coordination structure could affect Mg²⁺-binding affinity and Mg²⁺-inducible structural changes. Moreover, it would affect subsequent Ca²⁺ binding and Ca²⁺-inducible structural change. Differences

in the Mg^{2+}/Ca^{2+} coordination forms, Mg^{2+}/Ca^{2+} -affinities, and the conformational changes induced by Mg^{2+}/Ca^{2+} ions may be involved in the regulation of the various functions of NtCaM proteins.

In this study, I observed differences in the secondary and coordination structures of three types of NtCaM isoforms using FT-IR. Among them, NtCaM13 may have a partially unfolded structure compared to NtCaM1 and NtCaM3. I also revealed that NtCaM13 significantly changes its conformation upon Mg²⁺ binding and may have few unfolded domains in the Ca²⁺-bound form. These structural differences may affect their physiological activities.

Table I-1 FTIR marker bands appearance among Ca²⁺-binding proteins

	M	Marker bands		
	I	II	III	_
Bovine brain CaM	+	+	+	(Trewhella <i>et al.</i> 1989; Nara <i>et al.</i> 1995; Fabian <i>et al.</i> 1996)
NtCaM1	+	+	+	
NtCaM3	+	+	+	
NtCaM13	±	+	+	
Parvalbumin	_	+	+	(JACKSON <i>et al.</i> 1991; NARA <i>et al.</i> 1994)
Akazara scallop TnC	_	+	+	(Yuмото <i>et al</i> . 2001)
Turky TnC	+	+	+	(Trewhella <i>et al.</i> 1989)

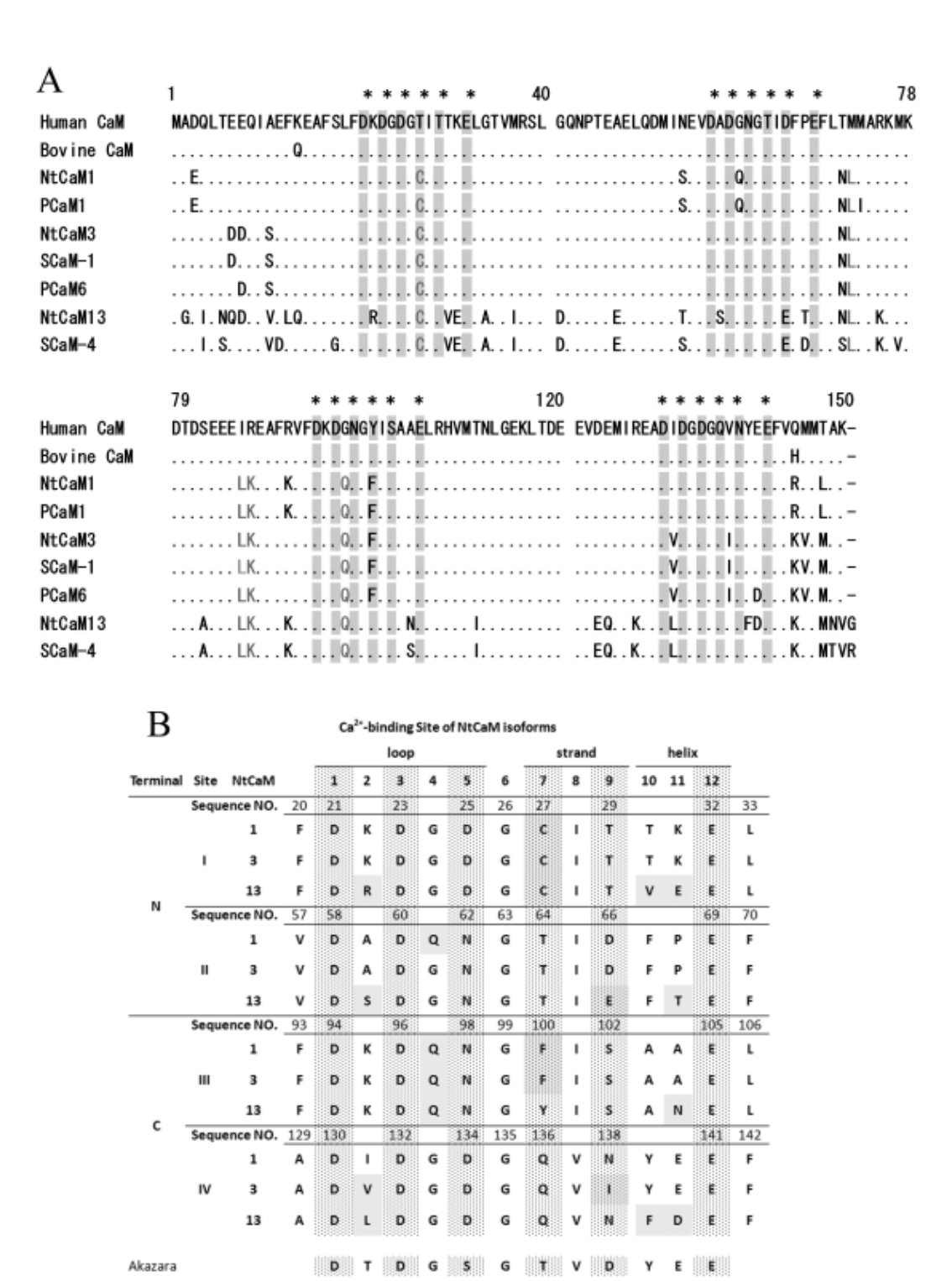


Figure I-1. Amino acid sequences of three types of NtCaMs. (A) Amino acid sequence comparison of three types of plant-specific CaMs and vertebrate CaMs. Dots indicate amino acids identical to those of vertebrate CaM. Asterisks indicate four conserved Ca²⁺ binding motifs, EF-hands, in which six residues at positions 1(X), 3(Y), 5(Z), 7(-Y), 9(-X) and 12(-Z) provide oxygen ligands to Ca²⁺. (B) EF-hand motifs in NtCaMs. Residues not common among the three types at each site are shown in gray.

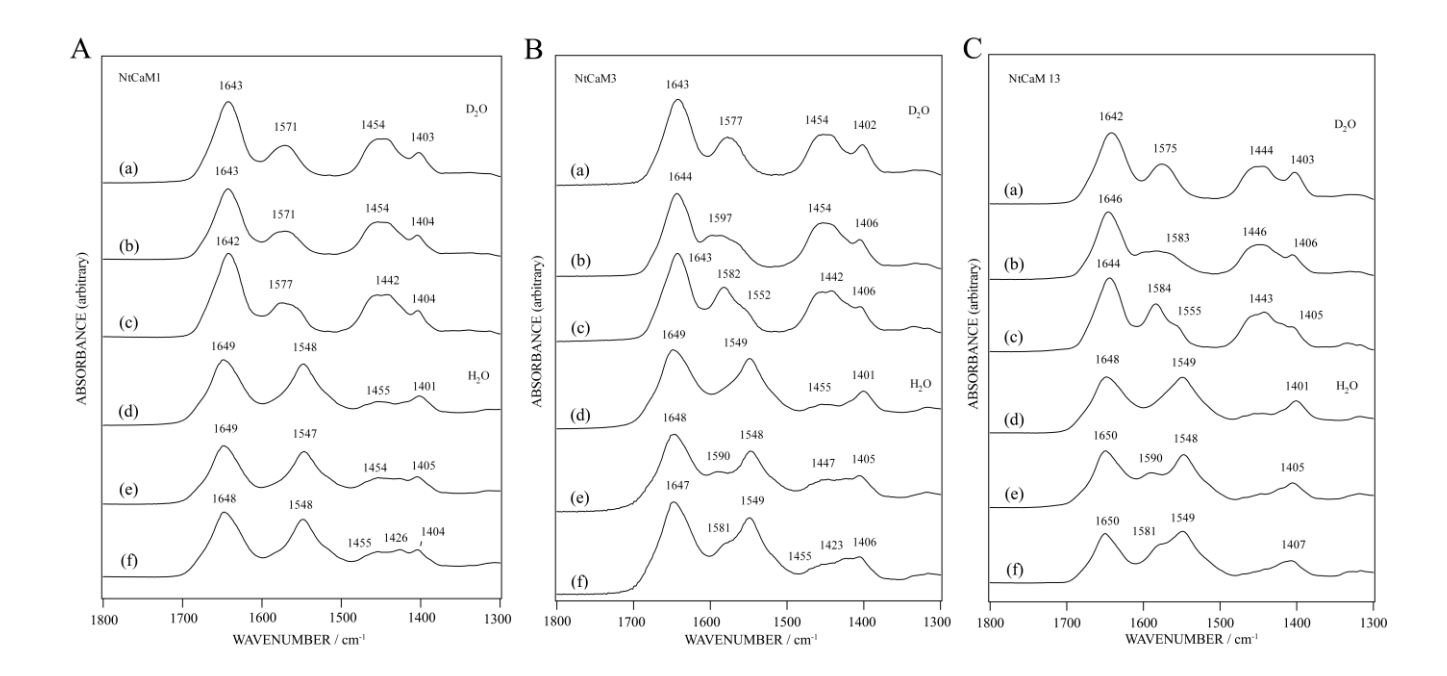


Figure I-2. Infrared spectra (1800–1300 cm⁻¹) of NtCaM1 (A), NtCaM3 (B) and NtCaM13 (C). (a), (b) and (c) in each panel were measured in D_2O , and (d), (e) and (f) were measured in H_2O . (a) and (d) in each panel were in the apo form, (b) and (e) in the Mg^{2+} -bound form, and (c) and (f) in the Ca^{2+} -bound form.

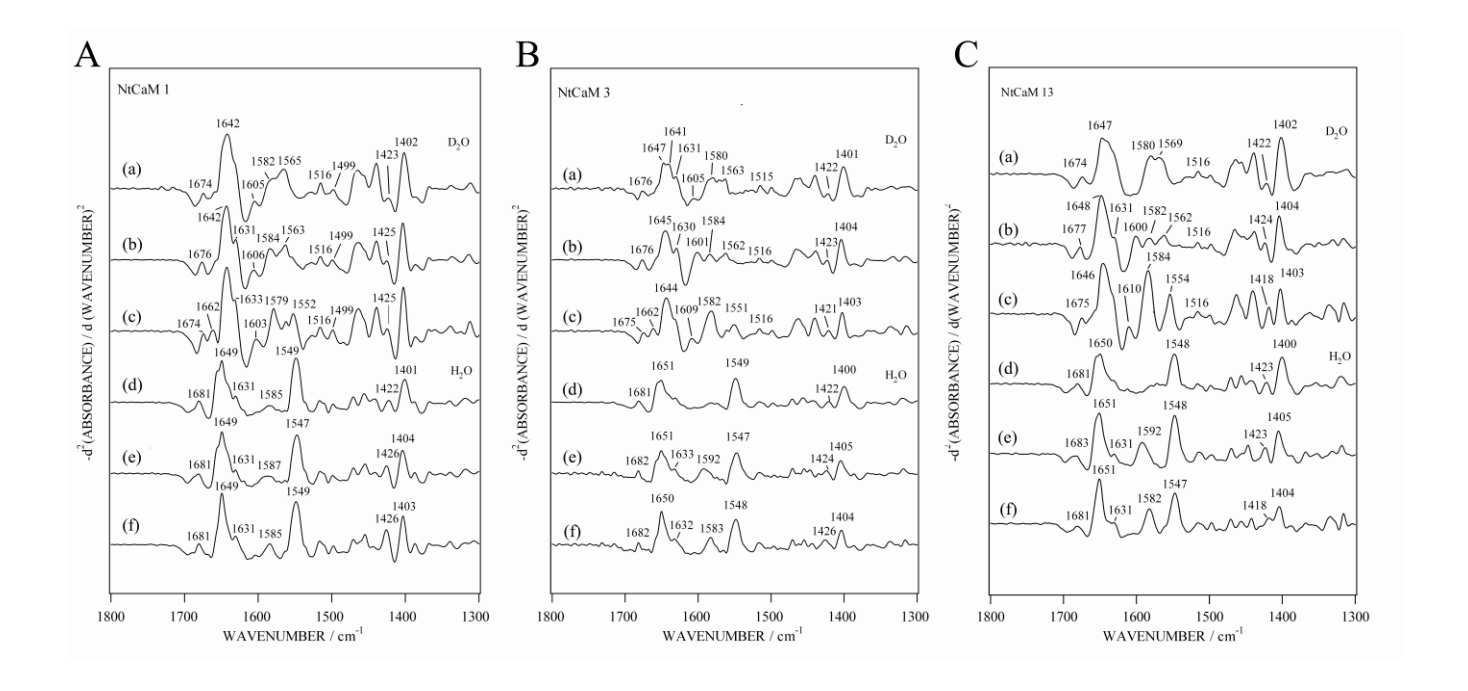


Figure I-3. Second-derivative spectra (1800–1300 cm⁻¹) of NtCaM1 (A), NtCaM3 (B) and NtCaM13 (C), corresponding to the infrared spectra in Fig. I-2. (a) and (d) are spectra of the apo form, (b) and (e) are spectra of the Mg²⁺-bound form and (c) and (f) are spectra of the Ca²⁺ bound form. (a), (b) and (c) are spectra in D₂O, and (d), (e) and (f) are spectra in H₂O.

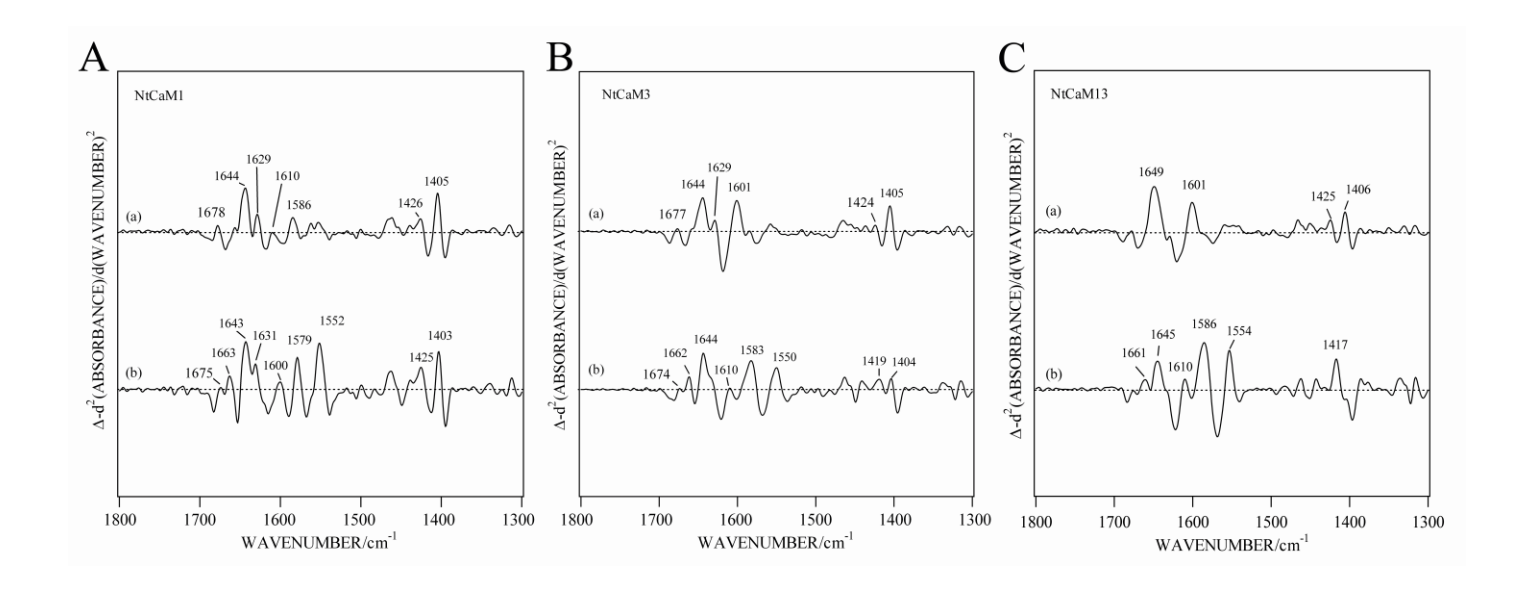


Figure I-4. Amplitude-difference spectra of NtCaM isoforms. Spectra were obtained by subtracting the second-derivative spectra of the apo forms of NtCaM1 (A), NtCaM3 (B) and NtCaM13 (C) from the second-derivative spectra of either the Mg²⁺-bound form ((a) in each panel) or the Ca²⁺-bound form ((b) in each panel) of the respective NtCaM. The second derivative band at 1515 cm⁻¹ was used as an internal standard since it is due to the CC-stretching mode of the tyrosine ring, not the Ca²⁺ ligand.

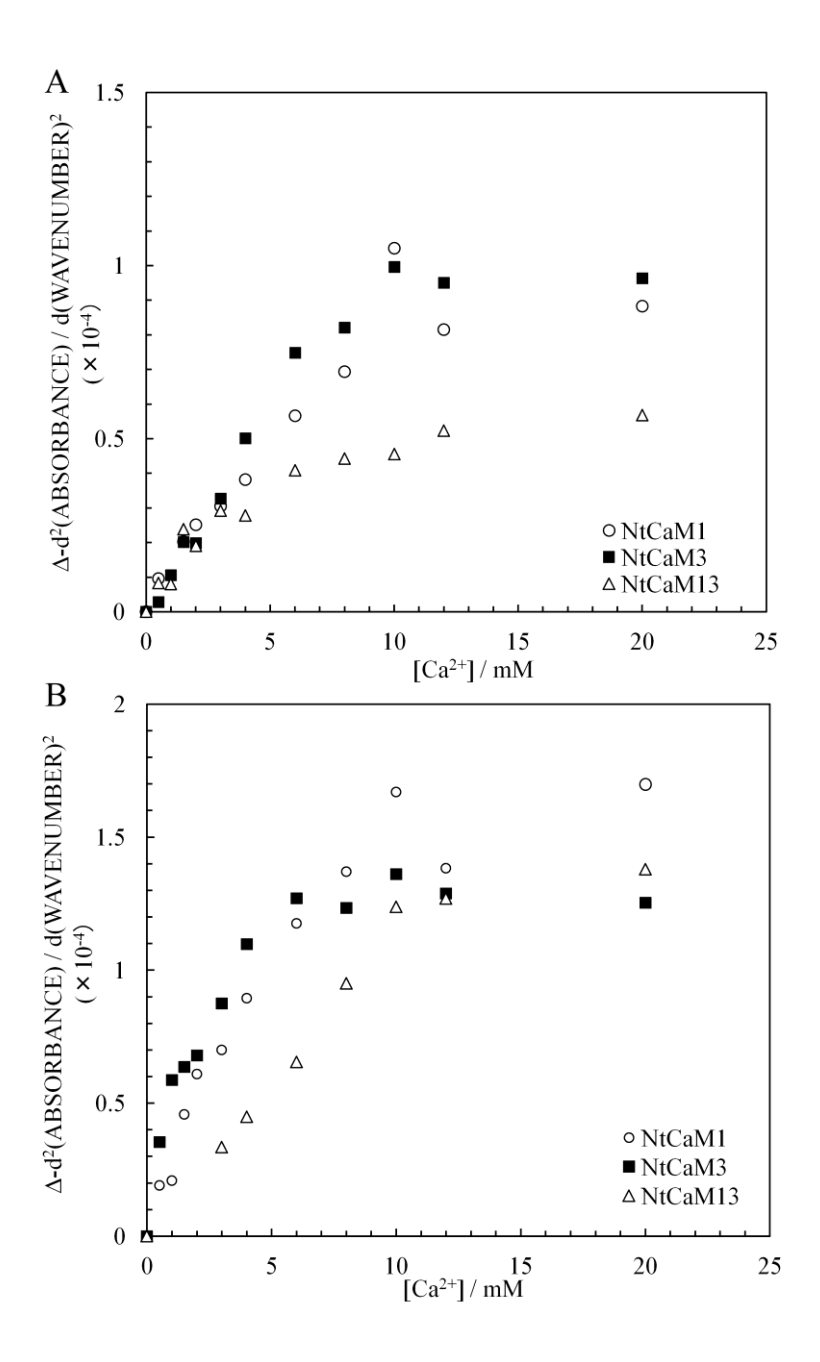


Figure I-5. Ca²⁺-dependent amplitudes of marker bands I (A) and II (B). The differences between the second-derivative spectra of Ca²⁺-bound NtCaM and apo NtCaM were obtained using the second derivative band at 1515 cm⁻¹ as an internal standard, as described in the legend to Figure I-4.

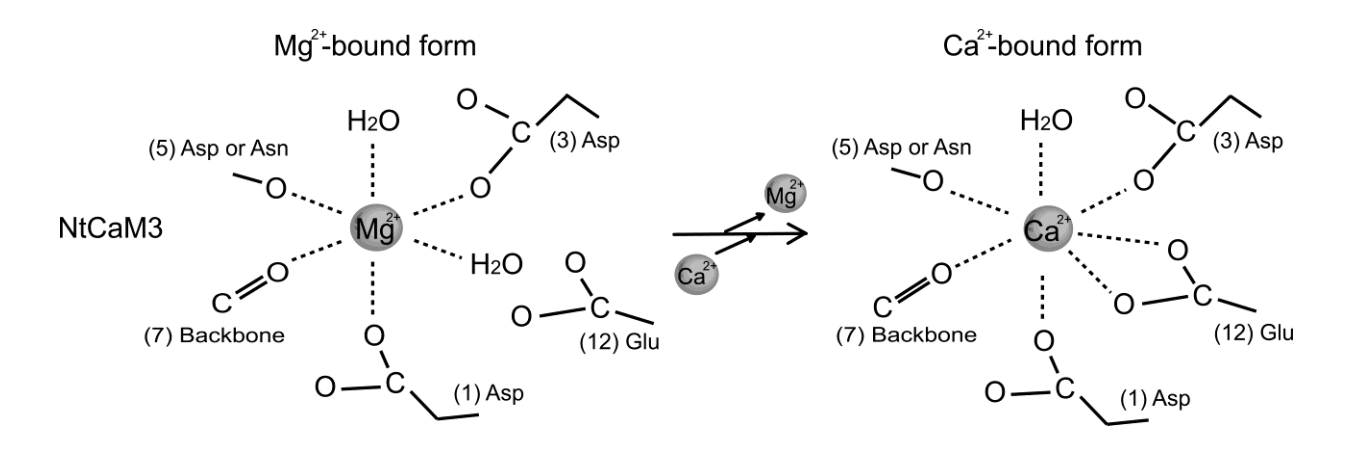


Figure I-6. Mg²⁺ and Ca²⁺ coordination model of NtCaM3. Asp residues at 1st, 3rd and 5th in each EF-hand site bind Mg²⁺ in pseudo-bridging mode while 12th Glu residues do not. However, 12th Glu residues contribute to Ca²⁺ binding in bidentate mode. Coordination structure of NtCaM13 may be similar to that of NtCaM3.

CHAPTER II

Calcium-dependent structural changes in human reticulocalbin-1

Summary

Human reticulocalbin-1 (hRCN1) has six EF-hand motifs and binds Ca^{2+} . hRCN1 is a member of the CREC family localized in the secretory pathway, and its cellular function remains unclear. In this study, I established a new bacterial expression and purification procedure for hRCN1. I observed that hRCN1 binds Ca^{2+} in a cooperative manner and the Ca^{2+} binding caused an increase in the α -helix content of hRCN1. On the other hand, hRCN1 did not change the structure with Mg^{2+} loading. hRCN1 is a monomeric protein, and its overall structure became more compact upon Ca^{2+} binding, as revealed by gel filtration column chromatography and small angle X-ray scattering. This is the first report of conformational changes in the CREC family upon Ca^{2+} binding. My data suggest that CREC family member interactions with target proteins are regulated in the secretory pathway by conformational changes upon Ca^{2+} binding.

Key words: Ca²⁺-binding; CREC family; EF-hand motif; human reticulocalbin-1; small angle X-ray scattering

1. Introduction

Reticulocalbin-1 (RCN1) is a member of the CREC family, which includes Cab45, RCN1, ERC-55, and calumenin (HONORE and VORUM 2000; HONORE 2009). The members are localized in the secretory pathway and have multiple EF-hand motifs. RCN1 was first cloned in mice, and the murine RCN1 (mRCN1) precursor polypeptide consists of 325 amino acid residues (OZAWA and MURAMATSU 1993). The 23 amino acid N-terminal region is a putative signal peptide, and accordingly, the mature mRCN1 polypeptide consists of 302 amino acid residues (from 24 to 325) (OZAWA and MURAMATSU 1993). mRCN1 has one N-glycosylation site at Asn-47, and a portion of mRCN1 was shown to be N-glycosylated (OZAWA and MURAMATSU 1993). mRCN1 has the endoplasmic reticulum (ER) retention signal HDEL at its C-terminus and was reported to be localized in the ER (OZAWA and MURAMATSU 1993). In addition, mRCN1 has six EF-hand motifs (Ozawa and Muramatsu 1993). EF-3 and EF-4 do not bind Ca²⁺, but the others do (TACHIKUI et al. 1997) (see Fig. II-2A). The human RCN1 (hRCN1) precursor polypeptide consists of 331 amino acid residues and is highly homologous (95% identity) to mRCN1 (OZAWA 1995). hRCN1 has the same structural features as those described for mRCN1, but it is not yet known whether all six EF-hands are functional or whether hRCN is N-glycosylated. hRCN1 has been reported to be localized in the Golgi complex (TSUKUMO et al. 2009). The N-terminus of the hRCN1 mature polypeptide was biochemically determined to be Ala-30, and the N-terminal 29 amino acid region is a signal peptide. The mature hRCN polypeptide consists of 302 amino acid residues (from 30 to 331) (TSUKUMO et al. 2009). A Pro residue, located second from the N-terminus of the mature hRCN1 polypeptide, is an ER export signal

(TSUKUMO et al. 2009). mRCN1 also has Pro-25, which corresponds to the hRCN1 ER export signal (Fig. II-2A), but it has not been reported whether Pro-25 of mRCN1 functions as an ER export signal. Recent studies demonstrated that hRCN1 is also localized on the cell surface in several endothelial cell lines, including bone marrow endothelial cells as well as several prostate cancer cell lines (COOPER et al. 2008). Moreover, hRCN1 cell surface expression in the endothelial cells is up-regulated by tumor necrosis factor-α (COOPER et al. 2008). hRCN1 up-regulation has also been reported in several cancer cells (YOSHIDA et al. 2011), but its cellular functions remain unclear. One putative function of CREC members is to bind and store Ca²⁺ in the secretory pathway. Ca²⁺-binding proteins in the ER, such as calnexin, calreticulin, calsequestrin, endoplasmin, and Erp72, generally show low affinity for Ca²⁺, in contrast to the high affinity of cytosolic Ca²⁺-binding proteins such as troponin C, calmodulin, parvalbumin, and intestinal Ca²⁺-binding protein (STRYNADKA and JAMES 1989; HONORE and VORUM 2000). The Ca²⁺-binding affinity of bacterially expressed human calumenin (hCalumenin) is low $(1.6 \times 10^3 \text{ M}^{-1})$ (VORUM et al. 1998), and thus it is supposed that CREC members are low-affinity Ca²⁺-binding proteins. In the secretory pathway, the free Ca²⁺ concentration is in the mM range (MELDOLESI and POZZAN 1998); thus, the involvement of CREC members in the binding and storing of Ca²⁺ is possible.

Information on CREC structures is scarce, because structural analyses on RCN1, as well as other CREC members, have not been performed. In the present study, I established an *Escherichia coli* expression system and purification method for hRCN1 and analyzed the higher order structures of hRCN1 with respect to Ca²⁺ binding.

2. Materials and methods

hRCN1 plasmid construction

A cDNA for hRCN1 was purchased from Open Biosystems (GenBank: BC010120). The gene encoding the mature hRCN1 polypeptide (residues 30–331) was amplified by PCR using the hRCN1 cDNA as a template. The PCR product was cloned into pGEM-T easy vector (Promega), and the sequence was confirmed to be correct. The NdeI-XhoI fragment of the correct plasmid was ligated into pColdTF (Takara) digested with the same enzymes.

Expression and purification of hRCN1

The *Escherichia coli* strain BL21(DE3) transformed with pColdTF-hRCN1 was cultured to an absorbance of 0.6 at 600 nm in Luria Broth containing 100 μg/mL ampicillin at 37°C. Protein expression was induced with 0.2 mM isopropyl β-D-1-thiogalactopyranoside at 16°C for 20 h. Cells were harvested by centrifugation at 5,000 g at 4°C for 10 min, suspended in 50 mM Tris-HCl (pH 8.0), and disrupted 4 times (30 s each sonication) with an ultrasonic disruptor (TOMY, Tokyo) at 40 W with 1-min intervals on ice. The sonicated suspension was centrifuged at 20,000 g at 4°C for 20 min. The supernatant was loaded onto a column packed with His-Bind resin (Novagen) equilibrated with 5 mM imidazole, 500 mM NaCl, and 20 mM Tris-HCl (pH 7.9), and the flow-through fraction was collected. The column was washed with 10 volumes of the same buffer of the resin and eluted with 6 volumes of 60 mM imidazole, 500 mM NaCl, and 20 mM Tris-HCl (pH 7.9). The elution fraction containing hRCN1 was dialyzed at 4°C overnight against 50 mM Tris-HCl, 100 mM NaCl, and 5 mM CaCl₂ (pH 8.0). Factor Xa (Novagen) was added to the dialysate to obtain a final ratio

of 0.005 U of enzyme to 1 µg of protein in the dialysate. Factor Xa digestion was performed at 20°C for 6 h. The digestion was stopped by addition of 4-(2-aminoethyl) benzenesulfonyl fluoride hydrochloride (AEBSF, Roche) to a final concentration of 2 mM. The digests were centrifuged for 10 min at 20,000 g. The supernatant was concentrated with Amicon Ultra-4 (30K cutoff, Millipore) and subjected to gel filtration column chromatography on Superdex 200 10/300 GL (GE Healthcare). The elution buffer was 25 mM Tris-HCl, 150 mM NaCl, and 2 mM CaCl₂ (pH 7.5) for Ca²⁺-bound hRCN1, and the flow rate was 0.4 mL/min. The fractions containing hRCN1 were combined, concentrated, and subjected to a second cycle of gel filtration column chromatography on Superdex 200 10/300 GL as described above. For preparation of apo hRCN1, purified Ca²⁺-bound hRCN1 was dialyzed for 16 h at 4°C against 25 mM Tris-HCl (pH 7.5), 150 mM NaCl, and 10 mM EDTA and then against 25 mM Tris-HCl (pH 7.5) and 150 mM NaCl for 16 h. As an alternative purification method, hRCN1 digested with Factor Xa as described above was incubated for 10 min at 80°C, followed by centrifugation at 20,000 g for 20 min at 4°C. The supernatant was subjected to gel filtration column chromatography on Superdex 200 10/300 GL as described above.

The protein concentration of hRCN1 was determined by absorption at 280 nm using 46410 M⁻¹ cm⁻¹ as a molar absorption coefficient and 34 kDa as the calculated molecular mass, according to the reported method (PACE *et al.* 1995).

SDS-PAGE

SDS-PAGE was performed on a 12.5% (w/v) separating gel according to the Laemmli method (LAEMMLI 1970). Standard proteins with a broad molecular mass

range (Bio-Rad and Takara) were used to estimate protein molecular masses, and the gels were stained with Coomassie brilliant blue.

CD spectroscopy

CD data in the range of 200–260 nm were collected at room temperature with 0.2-nm step resolution at a rate of 100 nm min⁻¹, a response time of 1 s, a bandwidth of 1.0 nm, and a scan number of 8 on a Jasco J-850 spectropolarimeter using quartz cuvette with a light path-length of 1 mm. Apo hRCN1 was dialyzed for 16 h at 4°C against 5 mM MOPS-KOH (pH 7.5) and 50 mM KCl and then concentrated with Amicon Ultra-4. The protein solution was adjusted to 10 μM hRCN1, 5 mM MOPS-KOH (pH 7.5), 50 mM KCl, and 2 mM EDTA (apo form); 2 mM CaCl₂ (Ca²⁺-loaded form); or 2 mM MgCl₂, SrCl₂, or BaCl₂ (other metal cation-loaded form). The effect of Ca²⁺ concentration on the hRCN1 spectrum was examined by adding various amounts of CaCl₂ to the apo hRCN1 solution dialyzed against 10 mM MOPS-KOH (pH 7.5). The final protein solutions consisted of 10 μM hRCN1, 5 mM MOPS-KOH (pH 7.5), and 0 to 10.0 mM CaCl₂. The CD spectra of hRCN1 were corrected by subtracting the corresponding spectra of buffers in the absence of protein.

The α -helix content was calculated using the two equation reported by Greenfield and Fasman (Greenfield and Fasman 1969) and Chen *et al.* (CHEN *et al.* 1972).

Fluorescence spectroscopy

Fluorescence spectra were acquired at room temperature on an F-2000 Fluorescence Spectrophotometer (Hitachi). Intrinsic emission spectra were obtained at

an excitation wavelength of 295 nm and scanned from 300 to 400 nm. When the effect of various metal cations on the fluorescence spectra was examined, the protein solution composition was adjusted to 10 μM hRCN1, 5 mM MOPS-KOH (pH 7.5), 50 mM KCl, and 2 mM of EDTA, CaCl₂, MgCl₂, SrCl₂, or BaCl₂. When the effect of various Ca²⁺ concentrations on the fluorescence spectra was examined, the protein solution composition was adjusted to 10 μM hRCN1, 5 mM MOPS-KOH (pH 7.5), 50 mM KCl, and various concentrations of CaCl₂, 0 to 10 mM. 8-Anilino-1-naphthalenesulfonic acid (ANS) fluorescence experiments were conducted with samples containing 10 μM hRCN1, 100 μM ANS, 5 mM MOPS-KOH (pH7.5), 50 mM KCl with 2 mM of EDTA, CaCl₂, SrCl₂, MgCl₂, or BaCl₂. When the effect of various Ca²⁺ concentrations on the ANS fluorescence was examined, the protein solution composition was adjusted to 10 μM hRCN1, 100 μM ANS, 5 mM MOPS-KOH (pH 7.5), 50 mM KCl, and various concentrations of CaCl₂, 0 to 10 mM. The excitation wavelength was 370 nm and the emission was recorded from 400 to 600 nm.

Isothermal Titration Calorimetry (ITC)

ITC experiments were performed at 25 °C on an iTC₂₀₀ microcalorimeter (GE Healthcare). hRCN was dialyzed against 10 mM Pipes-NaOH (pH 6.8) containing 100 mM NaCl. For Ca²⁺-titration, the sample cell was filled with 204 μ L of 100 μ M hRCN1 solution and 26 consecutive 1.5 μ L aliquots of the outer dialysate containing 4 mM CaCl₂ were injected at 120s intervals. For Mg²⁺-titration, the sample cell was filled with 204 μ L of 122 μ M hRCN1 solution and 26 consecutive 1.5 μ L aliquots of the outer dialysate containing 6 mM MgCl₂ were injected at 120 s intervals. Data analysis was performed using the Origin-ITC analysis package (GE Healthcare) in "one set of sites"

or "sequential binding" modes. The appropriateness of the modes was evaluated by the χ^2 value of curve fitting.

Limited proteolysis by trypsin and chymotrypsin

Digestion of hRCN1 by trypsin or chymotrypsin was performed at 25 °C in 25 mM Tris-HCl (pH 7.5), 150 mM NaCl, and 2 mM CaCl₂ in the presence of trypsin or chymotrypsin at the enzyme/substrate ratio of 1/100 (w/w) (Fig. II-7A). The time course of digestion was monitored by SDS-PAGE on 12.5 % separating gels. Digestion was stopped by adding AEBSF. Tryptic and chymotryptic fragments were separated by gel filtration column chromatography on Superdex 200 10/300 GL.

Digestion of hRCN1 by trypsin or chymotrypsin was also performed at 25 °C in 25 mM Tris-HCl (pH 7.5), 150 mM NaCl, and 2 mM of CaCl₂, SrCl₂, MgCl₂, BaCl₂ or EDTA in the presence of trypsin or chymotrypsin at the enzyme/substrate ratio of 1/1000 (w/w) or 1/250 (w/w), respectively (Fig. II-7B).

Protein sequencing

N-terminal sequences of purified hRCN1 and its tryptic and chymotryptic fragments were determined by automated Edman degradation using PPSQ-21 protein sequencer (Shimadzu).

Gel filtration experiment

Gel filtration of hRCN1 was performed on a Superdex 200 10/300 GL column at room temperature at a flow rate of 0.4 mL/min. The elution profile was monitored with a UV detector at 230 nm. The volume and the protein concentration of hRCN1 solution loaded to the column were adjusted to 100 μ l and 0.67 mg/ml, respectively, for

all conditions examined. The elution buffer was 25 mM Tris-HCl (pH 7.5) and 150 mM NaCl for analysis of apo hRCN1, and 2 mM of BaCl₂, MgCl₂, SrCl₂ or CaCl₂ was added to both the protein solution and the elution buffer for analysis of Ba²⁺, Mg²⁺, Sr²⁺ or Ca²⁺-loaded hRCN1, respectively.

Native-PAGE

Native-PAGE was performed on a 10 % (w/v) separating gel. hRCN1 solution (1 mg/ml) in 25 mM HEPES-KOH (pH 7.5), 100 mM KCl was used. Gels were run in 100 mM Tris-HCl (pH 7.8) for anode and 25 mM Tris, 192 mM Glycine for cathode at 15 mA. EDTA or Ca²⁺ was adjusted to 4 mM in both anode and cathode running buffers by adding 0.5 M EDTA or 1 M CaCl₂ to the buffers for the electrophoresis of hRCN1 in the absence or presence of Ca²⁺, respectively. BSA and ovalbumin were used as standard proteins to estimate protein mobilities. The gels were stained with Coomassie brilliant blue.

Small angle X-ray scattering (SAXS)

SAXS measurements were carried out at 20°C at Beam Line BL10C in the Photon Factory (Tsukuba, Japan). X-ray wavelength was 1.488 Å. Exposure time for each sample was 10 min. SAXS data were recorded using R-AXIS 7 detector (Rigaku) and camera length was 2 m. The samples were placed in a quartz sample cell with a path-length of 1.0 mm. hRCN1 solution was prepared in 25 mM Tris-HCl (pH 7.5), 150 mM NaCl, 2 mM CaCl₂ and 5% glycerol. CaCl₂ solution was added to each hRCN1 solution to give a final concentration of 12 mM for preparation of Ca²⁺-bound hRCN1, while EDTA solution was added to each hRCN1 solution to give a final concentration of 5 mM for preparation of apo hRCN1. Protein concentrations were adjusted to 0.5, 1.0,

1.5, 2.0, 2.5, 3.0, and 3.6 mg/ml for both Ca^{2+} -bound hRCN1 and apo hRCN1. Both apo and Ca^{2+} -buffers were also measured. Reduction of scattering images to one dimensional plots of intensity versus momentum transfer s (s= $4\pi \sin\theta/\lambda$, where 2θ is the scattering angle and λ the X-ray wavelength), was performed by FIT2D (http://www.esrf.eu/computing/scientific/FIT2D/, ESRF). Buffer subtraction was performed by Excel (Microsoft office). Buffer subtracted data were then analyzed using the ATSAS software package (Konarev *et al.* 2003; Petoukhov *et al.* 2007). Radius of gyration (R_g) values were determined from Guinier plot (s R_g < 1.3) using PRIMUS (Konarev *et al.* 2003; Konarev *et al.* 2006) and pair distance distribution function, P(r), was computed with the program GNOM (Svergun 1992). Definition of parameters used in this analysis is according to a literature (Putnam *et al.* 2007).

Low Resolution Shape Reconstruction

Ab initio molecular bead models of hRCN1 were generated using DAMMIF (FRANKE and SVERGUN 2009). Twenty independent DAMMIF models were aligned, averaged and filtered using DAMAVER (VOLKOVA and SVERGUN 2003).

3. Results and Discussion

Expression and purification of hRCN1

Soluble hRCN1 was expressed using pCold vector fused with trigger factor and then partially purified by His-Bind metal-chelating column chromatography utilizing the N-terminal His₆ tag (Fig. II-1A). At this step, the protein yield was 8 mg from 1 L culture. Previous reports successfully used maltose binding protein and

glutathione-S-transferase as N-terminal fusion proteins of mRCN1 to obtain soluble proteins (OZAWA and MURAMATSU 1993; TACHIKUI et al. 1997). However, the fusion proteins were not removed in the previous studies. In the present study, I found that trigger factor can be used to obtain soluble hRCN1. Trigger factor was cleaved by digestion with Factor Xa. I was unable to separate hRCN1 from trigger factor by hydroxyapatite, or hydrophobic column chromatography (data not shown). Because hRCN1 bound the metal-chelating resin by itself, I could not separate His6-tagged trigger factor from hRCN1 using the resin. Trigger factor was separated from hRCN1 by two cycles of gel filtration column chromatography on Superdex 200 (Fig. II-1A). As an alternative procedure, I found that hRCN1 remained soluble after incubation at 80°C for 10 min (Fig. II-1B). Trigger factor was recovered in the soluble supernatant after incubation at 40°C or 50°C (data not shown) but was insoluble after incubation at 60°C to 80°C (Fig. II-1B). Therefore, after treatment at 80°C for 10 min, trigger factor was separated from hRCN1 by centrifugation followed by one cycle of gel filtration column chromatography (Fig. II-1B). The yield of purified hRCN1 from 1 L culture was 4 mg. The N-terminal amino acid sequence was Arg-His-Met-Lys-Pro-Thr-Val, confirming that the purified protein was hRCN1 with an extra N-terminal Arg-His-Met derived from the vector. The data for structural characterization of hRCN1 purified by my primary method are shown. However, hRCN1 purified by my alternative method provided similar results (data not shown), suggesting that hRCN1 was not damaged by the heat treatment.

EF-hand motifs of hRCN1

Figure II-2A shows amino acid sequence of hRCN1 aligned with those of mRCN1 and hCalumenin. The horizontal bars with EF1 to EF7 show predicted EF-hand motifs of CREC family. In general EF-hand motifs, six residues at position 1st, 3rd, 5th, 7th, 9th, and 12th provide oxygen ligands to Ca²⁺ and these residues are indicated with deep gray (Figs. II-2, A and B). hCalumenin has seven predicted EF-hand motifs (EF1 to EF7 in Figure II-2A), while hRCN1 and mRCN1 have six EF-hand motifs EF2 to EF7. Gly in 6th position of EF-hand motif is conserved at a rate of 96% in general EF-hand motif (Fig. II-2B) (GIFFORD et al. 2007). The Gly residues in EF3, EF4 and EF7 are replaced by Asp, Leu, and Glu, respectively, in hRCN1 (Fig. II-2B). mRCN has similar replacements. EF7 of mRCN in which Gly is replaced by Glu can bind Ca2+ while EF3 and EF4, in which Gly residues are replaced by Glu and Leu, respectively, cannot bind Ca2+ (TACHIKUI et al. 1997). All of the seven EF-hand motifs in hCalumenin can bind Ca²⁺ despite the displacements of the 6th Gly residues in EF1 and EF4 to Ala and Leu, respectively (Fig. II-2B) (VORUM et al. 1998). Thus, the replacement of 6th Gly by Leu in EF4 is common among hRCN1, mRCN1 and hCalumenin, while the effects of the replacement on Ca²⁺-binding ability of EF4 are different between mRCN1 and hCalumenin. Considering the similarity between hRCN1 and mRCN1 sequences, EF3 and EF4 of hRCN1 might be also inactive.

Effect of divalent cations on the secondary structure of hRCN1

CD spectra of hRCN1 changed in a cation-specific manner (Fig. II-3A). Negative peaks at 208 and 222 nm clearly appeared in the presence of Sr^{2+} or Ca^{2+} , while the spectra of hRCN1 in the presence of Ba^{2+} and Mg^{2+} were similar to that of apo

hRCN1 (Fig. II-3A). α-Helix content was calculated according to two literatures by Greenfield and Fasman (GREENFIELD and FASMAN 1969) and Chen et al. (CHEN et al. 1972), then the content calculated according to the latter is shown in parentheses. Apo hRCN1 contained 23 (7) % α -helix and the α -helix content increased to 40 (30) and 43 (37) % in the presence of Sr^{2+} and Ca^{2+} , respectively, while the α -helix content of hRCN1 was 23 (7) and 24 (8) % in the presence of Mg²⁺ and Ba²⁺, respectively (Table II-1). These results indicate that hRCN1 bound both Ca²⁺ and Sr²⁺ and subsequently the α-helix content increased. In contrast, neither Ba²⁺ nor Mg²⁺ changed the secondary structure of hRCN1, suggesting that hRCN1 does not bind Mg²⁺ or Ba²⁺, otherwise binding of Mg²⁺ and Ba²⁺ did not change the secondary structure of hRCN1. Figure II-3B shows the Ca²⁺-dependent changes in the hRCN1 CD spectra. The Ca²⁺ concentration-dependent decrease in $[\theta]_{208}$ and $[\theta]_{222}$ indicates that the hRCN1 α -helix content increased with the increasing amounts of Ca²⁺. Apo hRCN1 contained 23 (7) % α-helix, and the content increased gradually to a plateau level around 42 (36) % in the presence of 0.36 mM Ca^{2+} (Table II-2). The plot of the $[\theta]_{222}$ against Ca^{2+} concentration showed that the Ca^{2+} concentration at 50% decrease in $[\theta]_{222}$ was estimated at 0.06 mM. (Fig. II-3B, inset). These results indicate that the hRCN1 secondary structure changes in Ca²⁺- and Sr²⁺-specific manners. Ionic radii of Mg²⁺, Ca²⁺, Sr²⁺ and Ba²⁺ are 0.72 (six coordination), 1.06, 1.21, and 1.38 (seven coordination) Å, respectively (SHANNON 1976). Ionic radius of Sr²⁺ is close to that of Ca²⁺ and therefore Sr²⁺ might bind hRCN1 and change the secondary structure in a similar manner to Ca²⁺.

Ca²⁺-dependent conformational changes of hRCN1

hRCN1 has six Trp residues (Fig. II-2A). Intrinsic Trp fluorescence spectra of hRCN1 at 300-400 nm with an excitation at 295 nm showed an increase in the maximum intensities (668.0 and 634.7) and downshifts in the maximum wavelength (336 nm and 339 nm) in the presence of Ca²⁺ and Sr²⁺, respectively, compared to the maximum intensity of 434.4 and the maximum wavelength of 345 nm for apo hRCN1 (Fig. II-4A). These spectral changes suggest that the hydrophobicity around Trp residues of hRCN1 increases in the presence of Ca²⁺ compared to that in the absence of Ca²⁺ and that the hydrophobicity around Trp in the presence of Sr²⁺ is similar to that in the presence of Ca²⁺ (ROYER 2006). However, the maximum intensities (440.0 and 439.2) and the maximum wavelengths (345 nm and 342 nm) of hRCN1 in the presence of Mg²⁺ and Ba²⁺, respectively, were similar to those of apo hRCN1 (Fig. II-4A). Together with the CD spectral results, these results suggest that hRCN1 preferentially binds Ca²⁺ over Sr²⁺ and the binding induces changes in the conformation of hRCN1 which leads to the changes in the environment around Trp residues. In contrast, hRCN does not bind Mg²⁺ or Ba²⁺, otherwise binding of Mg²⁺ and Ba²⁺ does not induce conformational change of hRCN1 at all. Ca²⁺-binding of hRCN1 caused an increase in the maximum intensity and a lower shift of the maximum wavelength of Trp fluorescence in a concentration-dependent manner (Fig. II-4B). The plot of the emission maximum intensity against Ca²⁺ concentration showed a sigmoidal curve (Fig. II-4B, inset), suggesting that conformational change around Trp residues of hRCN1 by Ca²⁺ binding to the EF-hand motifs is cooperative. The Ca²⁺ concentration at 50% increase in emission intensity was estimated at 0.06 mM.

Hydrophobic surface is exposed in apo form of hRCN1

The fluorescence probe ANS was used to detect exposed hydrophobic surfaces of hRCN1 (Fig. II-5). ANS itself shows a weak fluorescence in an aqueous solution. When it binds to hydrophobic area of proteins, its spectrum undergoes a noticeable blue shift and an increase in the emission intensity. When the fluorescence of ANS was observed for hRCN1 in the presence of various metal cations, the fluorescence intensity showed the order: $Ba^{2+} > Mg^{2+} > apo > Sr^{2+} > Ca^{2+}$ (Fig. II-5A), indicating that apo hRCN1 bound ANS more strongly than Sr²⁺-bound and Ca²⁺-bound hRCN1. This result suggests that hydrophobicity on the surface of apo hRCN1 is higher than those of Sr²⁺-bound and Ca²⁺-bound hRCN1. The ANS fluorescence intensity of Ca²⁺-bound hRCN1 was higher than that of ANS itself, suggesting that Ca²⁺-bound hRCN1 had hydrophobic surface which showed affinity for ANS. The ANS fluorescence changed in a Ca²⁺ concentration dependent manner in the presence of hRCN1 (Fig. II-5B), suggesting the Ca²⁺-dependent change in the hydrophobicity on the surface of hRCN1. The ANS fluorescence intensity decreased with the increasing Ca²⁺ concentration from 0.04 mM to 10 mM (Fig. II-5B), indicating that Ca²⁺-binding of hRCN1 caused conformational change which accordingly reduced hydrophobic surface. Interestingly Ba²⁺, Mg²⁺ and only 0.04 mM of Ca²⁺ among the concentrations examined enhanced ANS fluorescence compared to the fluorescence in the absence of metal cations (Figs. II-5, A and B). One possible reason is that apo hRCN1 formed hydrophobic intermolecular interaction which inhibited binding of ANS to apo hRCN1. Then, in the presence of Ba²⁺, Mg²⁺ or 0.04 mM Ca²⁺ the interaction between hRCN1 molecules was decreased and then ANS bound to hydrophobic surface on hRCN1 because Ba2+, Ca2+

and Mg^{2+} tend to decrease the strength of hydrophobic interaction and the effect has the order: $Ba^{2+} > Ca^{2+} > Mg^{2+}$ (QUEIROZ *et al.* 2001).

ITC measurements

I directly observed whether Mg²⁺ binds to hRCN1 by ITC (Fig. II-6A). Mg²⁺ bound to hRCN1 and the binding was endothermic. The curve for non-cooperative equivalent binding sites fitted best. The ITC result indicated that one hRCN1 molecule binds six Mg²⁺ ($N = 6.39 \pm 0.02$) with K_d value of 13.9 μ M (Table II-3). The binding enthalpy (ΔH) and entropy (ΔS) were 5.80 \pm 0.02 kcal mol⁻¹ and 41.7 cal mol⁻¹ deg⁻¹, respectively. The binding constants of hRCN1 for Ca²⁺ were also determined with ITC (Fig. II-6B). The Ca²⁺-binding of hRCN1 showed a mixed pattern of exothermic and endothermic. The curve for cooperative binding fitted best, showing that the result is consistent with the Ca^{2+} -dependent sigmoidal curve of $[\theta]_{222}$ and fluorescence. Although the thermodynamic parameters were not determined because of the low fitting accuracy of complicated curve, the K_d values were estimated for six Ca^{2+} -binding sites (Table II-3). The ITC result showed that one of six EF-hand motifs of hRCN1 is inactive for Ca^{2+} -binding (K_d value was 10.7 mM) and that K_d of hRCN1 was about 10^{-6} M for three high-affinity Ca²⁺-binding sites and 10⁻⁵ M for two low-affinity sites. The average K_d value is similar to the Ca²⁺ concentration (0.06 mM) giving 50% change in CD spectra and intrinsic Trp fluorescence. The K_d for Ca^{2+} binding to calmodulin was reported to be around $10^{-5} \sim 10^{-6}$ M, that of troponin C was about 10^{-7} M for high-affinity Ca²⁺-binding sites and 10⁻⁵ M for low-affinity sites, and that of parvalbumin was about 10-9 M (STRYNADKA and JAMES 1989). hCalumenin is the only member of CREC whose Ca2+-binding mode has been reported. Ca2+-binding of hCalumenin is non-cooperative and the K_d value was reported to be 0.6 mM (VORUM *et al.* 1998), while Ca^{2+} -binding of hRCN1 was cooperative and K_d values were in the same range of those of calmodulin. Thus, the Ca^{2+} -binding mechanisms might be different between hRCN1 and hCalumenin. Since the binding of Mg^{2+} to hRCN1 did not cause changes in CD spectra or intrinsic fluorescence, the binding sites of Mg^{2+} might be different from those of Ca^{2+} .

Ca^{2+} -bound hRCN1 is more resistant to proteolysis than Sr^{2+} -bound and apo forms

Figure II-7A shows time course of the tryptic and chymotryptic digestion of hRCN1 in the presence of Ca²⁺, Sr²⁺, or EDTA. Both trypsin and chymotrypsin digested Sr²⁺-bound and apo hRCN1 more effectively than Ca²⁺-bound hRCN1. Sr²⁺-bound hRCN1 was similar to apo form as to limited proteolysis. This suggests that Sr^{2+} -bound form was not rigid as Ca²⁺-bound form while the secondary and tertiary structures were similar between the two forms. For tryptic digestion of Ca²⁺-loaded hRCN1, one main band at 38 kDa and two minor bands at 35 kDa and 27 kDa were observed (Fig. II-7A, upper left panel). The two bands at 38 kDa and 27 kDa were purified by gel filtration column chromatography (data not shown) and the cleavage sites were determined to be between Lys⁷⁰ and Thr⁷¹ and between Lys¹⁷⁶ and Ala¹⁷⁷, respectively (Figs. II-2A and II-7B), by Edman degradation of each fragment. For chymotryptic digestion of Ca²⁺-bound hRCN1, two main bands at 38 kDa and 27 kDa were observed (Fig. II-7A, upper right panel) and the cleavage sites were between Phe⁷² and Asp⁷³ and between Phe¹⁶⁴ and Lys¹⁶⁵, respectively (Figs. II-2A and II-7B). These data indicate that in the presence of Ca2+ two regions upstream of EF2 and between EF3 and EF4 are susceptible to tryptic and chymotryptic digestion and the region consisting of EF4 to

EF7 is resistant to the digestion, while in the absence of Ca²⁺ the region from EF4 to EF7 becomes susceptible to the digestion.

Gel filtration and native-PAGE of hRCN1

The elution positions of hRCN1 on gel filtration column chromatography performed without or with addition of Ca²⁺ to the elution buffer were at 31.8 and 35.6 min, respectively (Fig. II-8). The apparent molecular masses, estimated according to the elution positions of standard proteins (data not shown), were 119 (apo hRCN1) and 48 kDa (Ca²⁺-loaded hRCN1). In addition, the apparent molecular masses of Ba²⁺ and Mg²⁺-loaded hRCN1 were 90 and 98 kDa, respectively, and these positions were similar to that of apo form. On the other hand, the apparent molecular mass of Sr²⁺-loaded hRCN1 was 48 kDa and similar to that of Ca²⁺-loaded hRCN1 (Fig. II-8). Native-PAGE of hRCN1 in the absence and presence of Ca²⁺ showed the result consistent with that of gel filtration, that is, the mobility of hRCN1 was smaller in the absence of Ca²⁺ than that in the presence of Ca²⁺ in comparison with the mobilities of BSA and ovalbumin as standards (Fig. II-9). These results suggest that the shape of hRCN1 changed dramatically depending on Ca²⁺.

Low-resolution structures of hRCN1

Structural changes of hRCN1 in solution upon Ca^{2+} -binding were also examined by SAXS. Figure II-10A shows the scattering curves of apo and Ca^{2+} bound hRCN1 in protein concentrations between 0.5 to 3.6 mg/ml. The scattering curves of apo form showed more straight and flat lines than those of Ca^{2+} -bound form and especially the curves of 3.6 mg/ml of apo hRCN1 showed higher intensities in low s values compared to those of Ca^{2+} -bound form (Fig. II-10A). R_g and I(0) were obtained

by Guinier plot and Gnom analysis (Table II-4) and $R_{\rm g}$ and I(0)/c were plotted against the protein concentration (Fig. II-10B). The $R_{\rm g}$ value of apo form was larger than that of Ca²⁺ bound form at any concentration examined and increased in a protein concentration-dependent manner (Fig. II-10B and Table II-4). The value of I(0)/c is proportional to molecular weight. The I(0)/c values at 1.5 were similar to each other in both apo and Ca2+-bound forms, but from 2 to 3.6 mg/ml the values of apo form increased in a protein concentration-dependent manner while the values of Ca2+-bound form did not change (Fig. II-10C). These results together with the result of gel filtration indicate that Ca²⁺-bound hRCN1 is a monomeric protein and does not form aggregates at high protein concentrations such as more than 3 mg/ml. On the other hand, apo hRCN1 is a monomeric protein with larger R_g value than that of Ca²⁺-bound hRCN1 at 0.5 and 1 mg/ml, suggesting that molecular shape of apo hRCN1 is different from that of Ca²⁺-bound hRCN1. At high concentration at more than 2 mg/ml apo hRCN1 is not a monomer and might form aggregates. The Kratky plot in Figure II-10D is derived from the data at 1 mg/ml and a prominent peak at low angle is shown in Ca²⁺-bound hRCN1 but not in apo hRCN1, indicating that hRCN1 is folded when bound to Ca2+ but is unfolded or only partially folded in the apo form (DONIACH 2001). Pair distance distribution function (Fig. II-10E) shows that apo hRCN1 has elongated shape compared to that of the Ca^{2+} -bound form as judged from the large D_{max} of apo hRCN1. Ab initio molecular bead model of Ca²⁺-bound form (Fig. II-10F) suggests that the Ca²⁺-bound form has mainly globular part but there is a projecting part in the upper part of the model. While the existence of small amount of the species often causes projecting in the upper arts of the model in shape reconstitution analysis by DAMMIF, this was a reproducible result. This part might be sensitive to tryptic and chymotryptic digestion.

This difference in molecular shape is consistent with the increase in apparent molecular mass in the absence of Ca²⁺ observed by gel filtration (Fig. II-8).

Cytosolic high-affinity Ca²⁺-binding proteins, such as calmodulin, parvalbumin, and troponin C, are known to bind Mg²⁺ (GRABAREK 2011). Mg²⁺ is thought to stabilize Ca²⁺-binding proteins under low Ca²⁺ conditions in resting cells (GRABAREK 2011). In a recent study, nuclear magnetic resonance data of soybean calmodulin 4 (sCaM4) indicated that apo sCaM4 possesses a half-unfolded structure, with the N-terminal domain unfolded and the C-terminal domain folded (HUANG et al. 2010). Mg²⁺ binding changes the unfolded structure to a well-folded structure for N-terminal domain of sCaM4 (HUANG et al. 2010). Mg²⁺ maintains the folded structure of sCaM4 in the absence of Ca²⁺ but does not activate sCaM4, whereas Ca²⁺ activates sCaM4 (HUANG et al. 2010). However, affinity of hRCN1 for Mg²⁺ was very low and Mg²⁺-loading to hRCN1 did not change the secondary structure or the tertiary structure of hRCN1. Instead, changes in hRCN1 structure were induced by Sr²⁺-loading. The binding of Sr²⁺ to hRCN1 may keep hRCN1 folded in the absence of Ca2+, although SAXS analysis of Sr²⁺-loaded hRCN1 was not performed in this study. Because apo hRCN1 was unfolded, as revealed by SAXS (Fig. II-10C), the effect of cation-binding on hRCN1 structure is similar to that on the N-terminal domain of sCaM4; both need cation-binding to keep their structures folded. More detailed structural analyses are necessary to clarify the questions why CREC family members hRCN1 and hCalumenin have different Ca²⁺-binding modes and why the binding of Mg²⁺ to hRCN1 does not affect hRCN1 structure.

Table II-1 α -Helix content of human reticulocalbin 1 loaded with various cations.

			α-Helix content	
	$[\Theta]_{208}$	[O] ₂₂₂	208nm	222nm
apo	-10720	-4390	23%	7%
Mg	-10780	-4520	23%	7%
Ba	-10860	-4890	24%	8%
Sr	-15290	-11470	40%	30%
Ca	-16400	-13410	43%	37%

Table II-2 Effect of Ca^{2+} concentration on α -helix content of human reticulocalbin 1.

			α-Helix content		
[Ca ²⁺]/mM	[0] ₂₀₈	[θ] ₂₂₂	208 nm	222 nm	
0	-10,650	-4,430	23%	7%	
0.01	-10,480	-4,330	22%	7%	
0.02	-10,580	-4,430	23%	7%	
0.03	-10,530	-4,390	23%	7%	
0.04	-10,970	-5,350	24%	10%	
0.05	-12,190	-7,020	28%	15%	
0.06	-13,010	-8,320	31%	20%	
0.08	-14,350	-10,350	36%	26%	
0.1	-14,840	-11,290	37%	30%	
0.12	-15,330	-11,960	39%	32%	
0.14	-15,530	-12,210	40%	33%	
0.16	-15,870	-12,510	41%	34%	
0.18	-15,850	-12,550	41%	34%	
0.3	-15,980	-12,850	41%	35%	
0.36	-16,240	-13,110	42%	36%	
0.4	-16,100	-13,100	42%	36%	
0.5	-16,170	-13,240	42%	36%	
1	-16,340	-13,170	43%	36%	
1.5	-16,220	-13,250	42%	36%	
2	-16,370	-13,430	43%	37%	
5	-16,420	-13,520	43%	37%	
10	-16,230	-13,370	42%	36%	

Table II-3 Dissociation constants of hRCN1 obtained by ITC measurements.

		K _d (M)			
Mg ²⁺ -loaded hRCN1	(1.39 ± 0.05) × 10 ⁻⁵		
	(7.28 ± 1.00) × 10 ⁻⁵		
	(5.17 ± 0.58	$) \times 10^{-6}$		
Ca ²⁺ -loaded hRCN1	(2.75 ± 0.36	$) \times 10^{-6}$		
Ca -loaded nRCN1	(4.60 ± 0.50	$) \times 10^{-6}$		
	(4.58 ± 0.40) \times 10 ⁻⁵		
	(1.07 ± 0.16	$) \times 10^{-2}$		

Table II-4 SAXS analysis data of $R_{\rm g}$ and I(0) at each analysis step.

sample	sample conc.		Guinire		Gnom		
	mg/ml	mM	Rg (Å)	<i>I</i> (0)	Rg (Å)	<i>I</i> (0)	D _{max} (Å)
apo RCN1	0.5	0.014	37.1 ± 0.2	24.00 ± 0.072	38.99 ± 0.09	24.22 ± 0.06	125.1
	1	0.028	39.6 ± 0.3	51.31 ± 0.26	39.33 ± 0.08	50.09 ± 0.12	132.1
	1.5	0.042	43.0 ± 0.2	87.00 ± 0.27	43.66 ± 0.12	86.06 ± 0.21	151.6
	2	0.056	47.5 ± 0.2	132.6 ± 0.31	47.6 ± 0.09	127.6 ± 0.28	156.4
	2.5	0.070	60.1 ± 0.3	227.52 ± 0.66	56.88 ± 0.17	212.5 ± 0.63	190.0
	3	0.084	65.3 ± 0.5	372.57 ± 2.25	72.31 ± 0.39	387.7 ± 2.01	269.9
	3.6	0.100	70.8 ± 0.5	592.34 ± 3.1	70.62 ± 0.22	574.3 ± 2.05	240.0
Ca RCN1	0.5	0.014	26.5 ± 0.07	30.84 ± 0.05	26.28 ± 0.03	30.37 ± 0.04	84.9
	1	0.028	26.8 ± 0.09	58.04 ± 0.13	26.76 ± 0.03	57.4 ± 0.07	87.6
	1.5	0.042	27.7 ± 0.07	89.87 ± 0.14	27.32 ± 0.04	88.55 ± 0.11	93.1
	2	0.056	27.8 ± 0.08	118.8 ± 0.20	26.5 ± 0.04	114.2 ± 0.17	86.4
	2.5	0.070	25.9 ± 0.08	141.7 ± 0.23	26.16 ± 0.03	141.6 ± 0.17	86.5
	3	0.084	26.8 ± 0.07	174.14 ± 0.25	27.58 ± 0.08	175.3 ± 0.32	104.6
	3.6	0.100	27.3 ± 0.07	214.58 ± 0.32	27.99 ± 0.08	215.6 ± 0.04	108.2

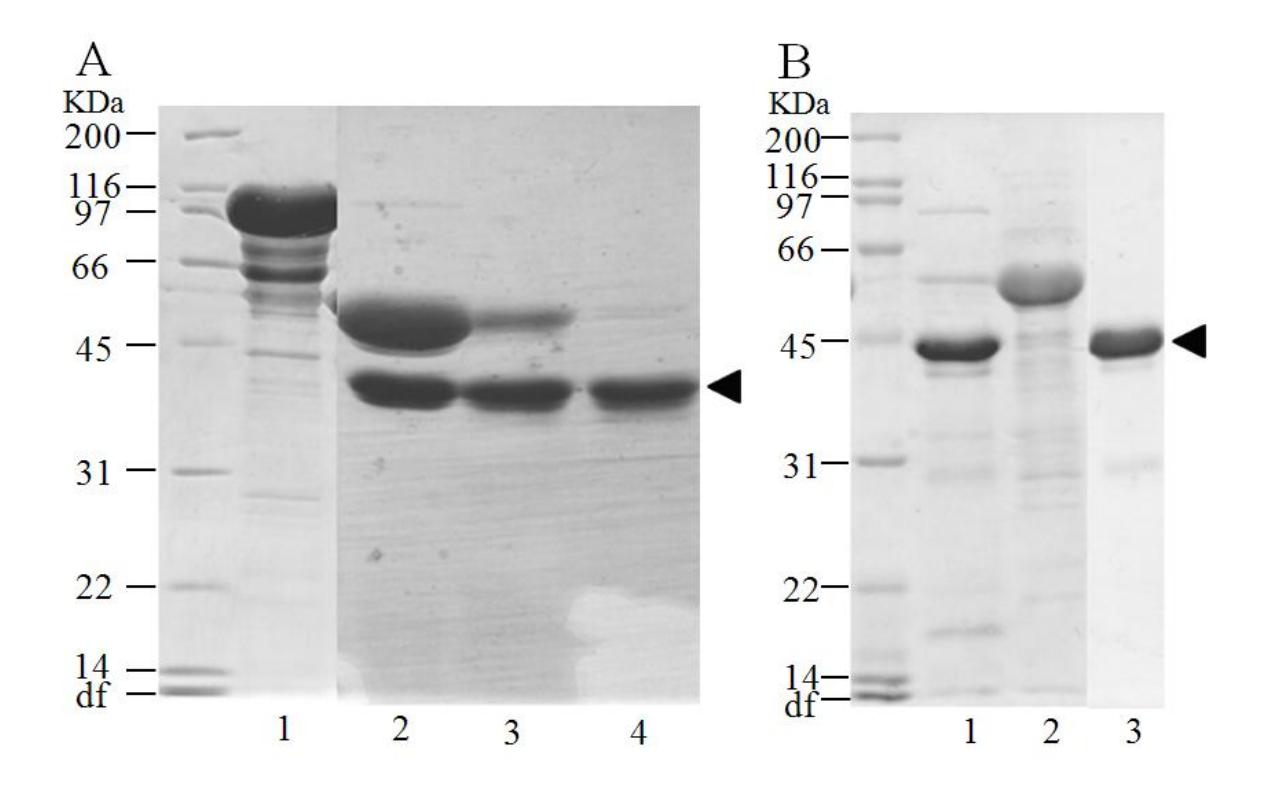


Figure II-1 SDS-PAGE analyses of human reticulocalbin 1 (hRCN1) purification steps. (A) Purification of hRCN1 by two cycles of gel filtration. hRCN1 was affinity-purified utilizing the N-terminal His₆ tag with metal-chelating resin (lane 1) and digested with Factor Xa (lane 2). The digests were fractionated with gel filtration column chromatography, and the combined fractions containing hRCN1 (lane 3) were subjected again to gel filtration to further remove trigger factor (lane 4). (B) An alternative purification procedure for hRCN1 using heat treatment. hRCN1 was purified with metal-chelating resin and digested with Factor Xa as described in (A). The digests were incubated at 80°C for 10 min and separated into supernatant (lane 1) and pellet (lane 2). The supernatant was subjected to gel filtration column chromatography to further purify hRCN1 (lane 3). The arrowheads indicate hRCN1. Molecular mass standards are shown on the left of each panel. df; dye front.

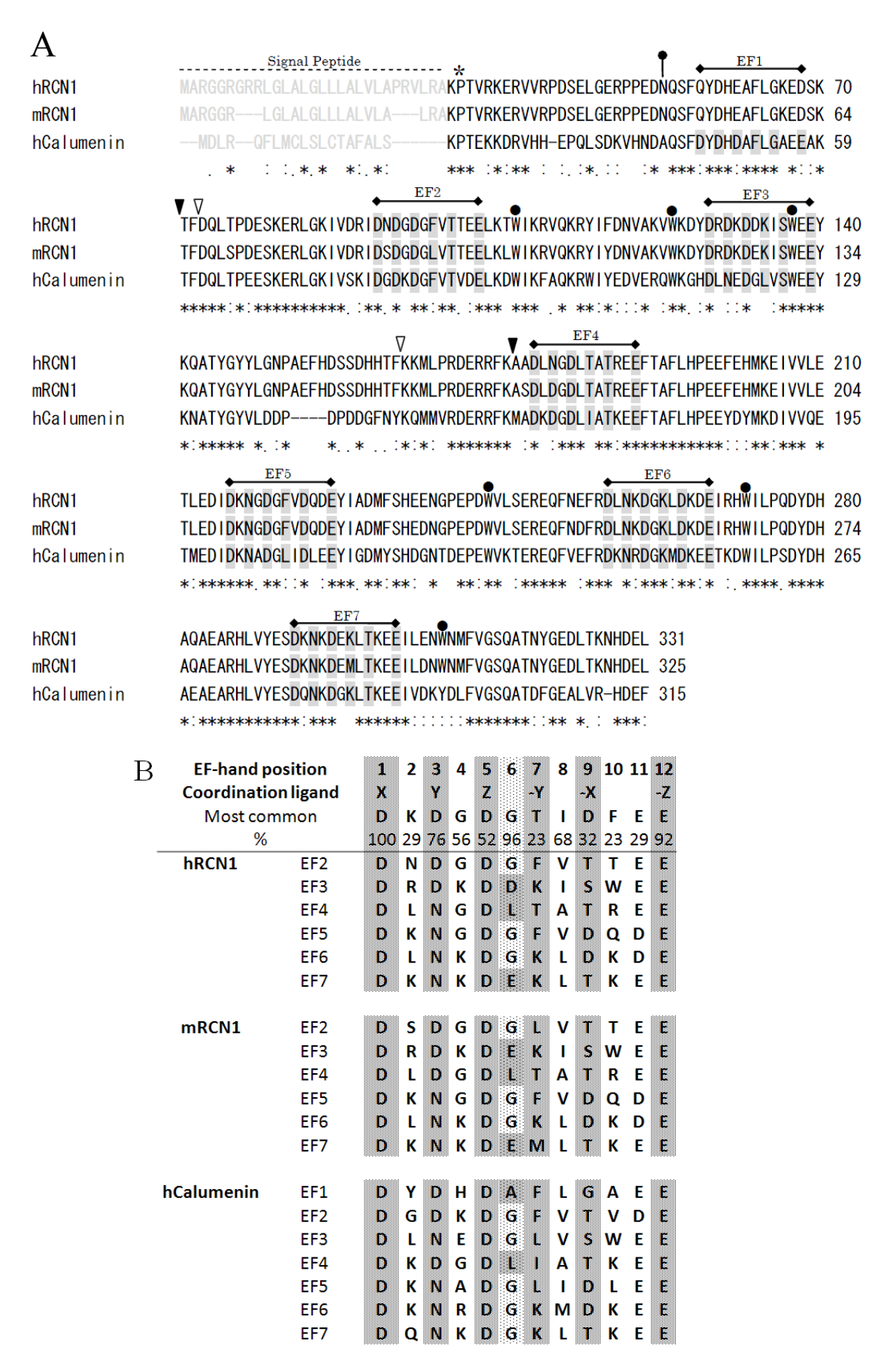


Figure II-2 Amino acid sequences of human reticulocalbin 1 (hRCN1) and mouse RCN1 (mRCN1) and human calumenin (hCalumenin). (A) Amino acid sequence comparison among hRCN1, mRCN1 and hCalumenin. N-terminal faint letters show signal peptide. Pro residues with an asterisk show the position of an ER export signal which was revealed in hRCN1 (TSUKUMO et al. 2009). Horizontal lines with EF1 to EF7 show predicted EF-hand motifs in hCalumenin. Six EF-hand motifs, EF2 to EF7, are predicted in hRCN1 and mRCN1. A black circle with a bar over Asn residues shows potential N-glycosylation site of hRCN1 and mRCN1. The potential site of mRCN1 is actually N-glycosylated (OZAWA and MURAMATSU 1993) but N-glycosylation of hRCN1 is not yet clarified. Black triangles indicate trypsin digestion sites and white triangles indicate chymotrypsin digestion sites (see Fig. II-3B). C-terminal four amino acid residues, HDEL and HDEF, are ER retention signals. Black circles indicate the position of six tryptophan residues. Asterisks under the sequences indicate residues fully conserved among the three proteins. Colons indicate residues of strongly similar properties. Periods indicate residues of weakly similar properties. This sequence alignment was performed with ClustalW2 (http://www.ebi.ac.uk/Tools/msa/clustalw2/) (B) EF-hand motifs in hRCN, mRCN1 and hCalumenin. Twelve residues contained in each of EF2 to EF7 for hRCN1 and mRCN1 and EF1 to EF7 for hCalumenin are aligned vertically. Residues at 1st, 3rd, 5th, 7th, 9th and 12th are involved in coordination and indicated with deep gray. Most common residues at each position with conservation levels in percentage (GIFFORD et al. 2007) are shown. At position 6, the residues other than the most common Gly are shown in light gray.

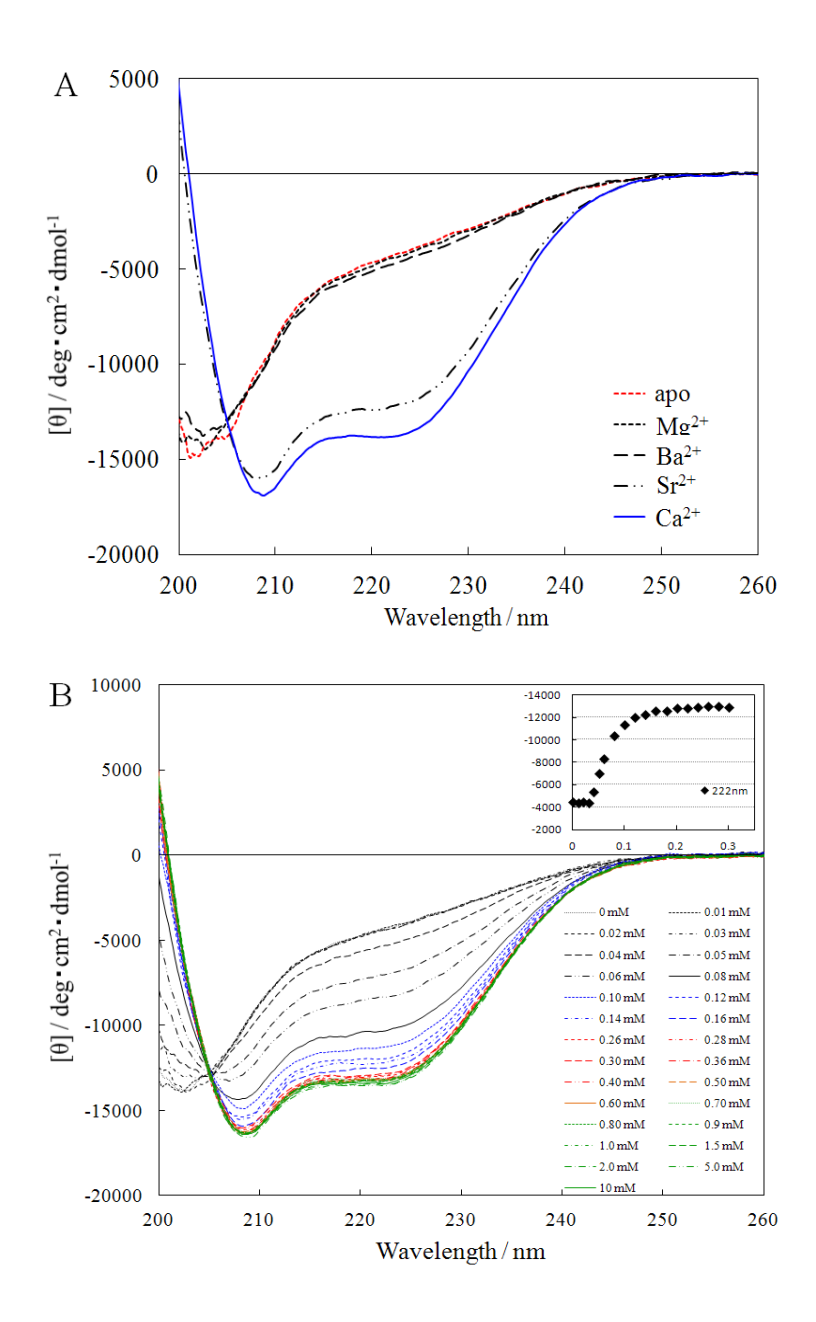


Figure II-3 CD spectra of human reticulocalbin 1 (hRCN1). (A) Effect of divalent metal cations on the CD spectra. The final protein solution consisted of 10 μM hRCN1, 5 mM MOPS-KOH (pH 7.5), 50 mM KCl, and 2 mM EDTA (apo form); 2 mM CaCl₂ (Ca²⁺-loaded form); and 2 mM MgCl₂, SrCl₂, or BaCl₂ (other metal cation-loaded forms). (B) Effect of various concentrations of Ca²⁺ on the CD spectra. The final protein solution consisted of 10 μM hRCN1, 5 mM MOPS-KOH (pH 7.5), 50 mM KCl, and 0 to 10 mM CaCl₂. Inset shows the Ca²⁺ concentration-dependent change in 222 nm intensity.

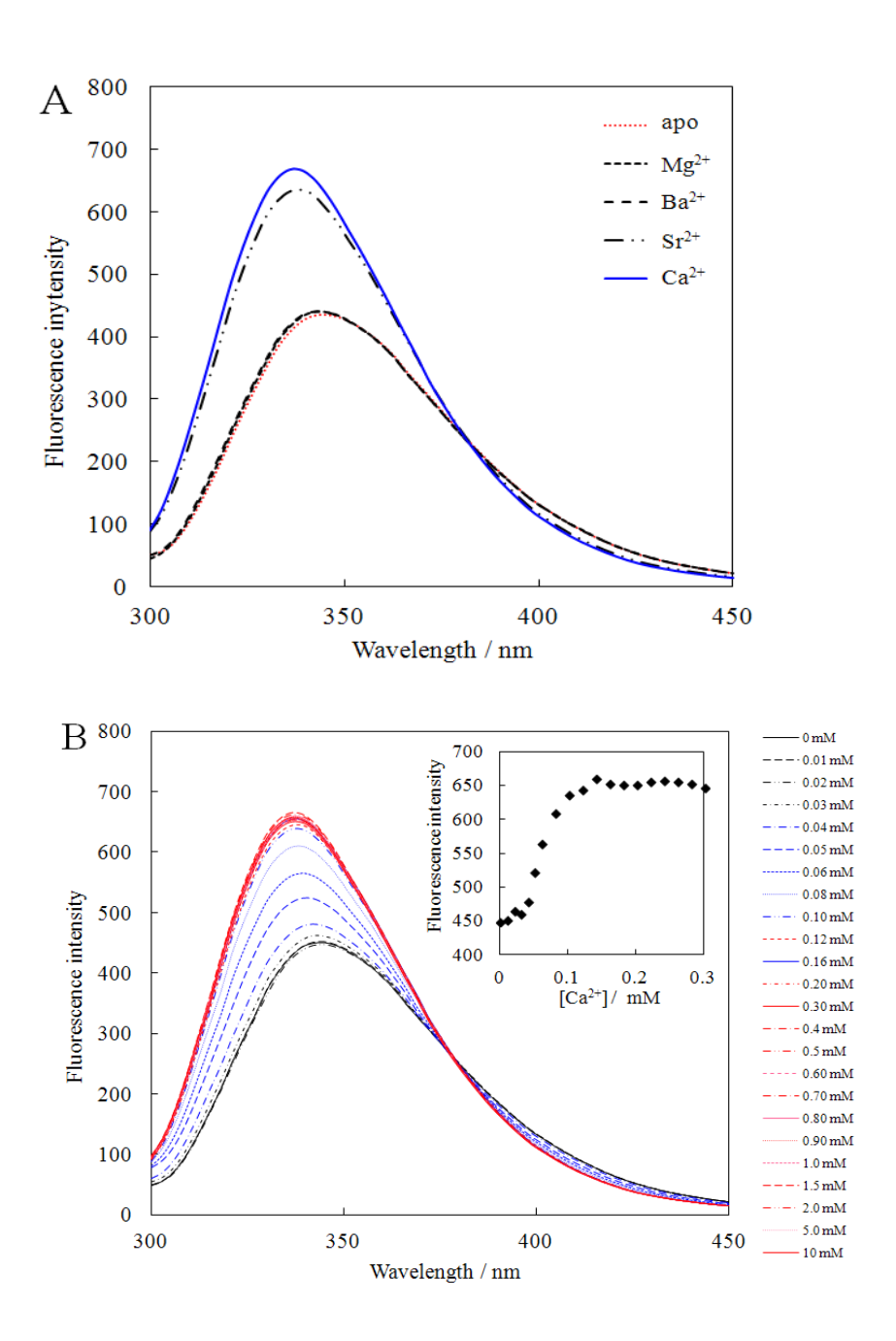


Figure II-4 Intrinsic fluorescence spectra of human reticulocalbin 1 (hRCN1). (A) Effect of divalent metal cations on intrinsic Trp fluorescence. The protein solution consisted of 10 µM hRCN1, 5 mM MOPS-KOH (pH 7.5), 50 mM KCl, and 2 mM of EDTA, CaCl₂, MgCl₂, SrCl₂, or BaCl₂. The excitation wavelength was 295 nm. (B) Effect of various Ca²⁺ concentrations on intrinsic Trp fluorescence. The protein solution consisted of 10 µM hRCN1, 5 mM MOPS-KOH (pH 7.5), 50 mM KCl, and various of CaCl₂ from 0 to 10 mM. Inset shows Ca^{2+} concentrations concentration-dependent change in the maximum fluorescence intensity. The Ca^{2+} performed reproducible experiments three times, and were concentration-dependent changes were obtained. A representative result is shown.

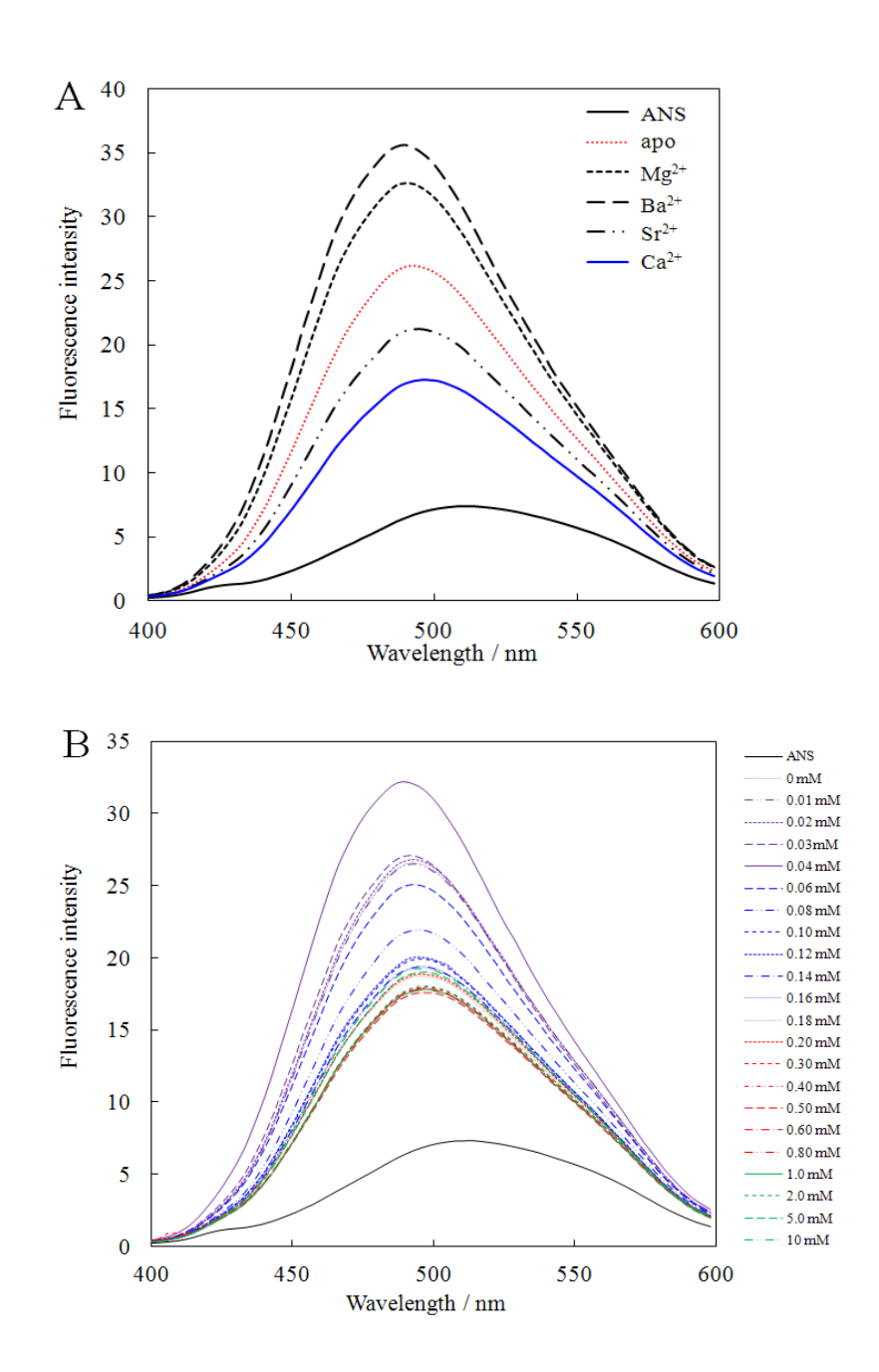


Figure II-5 8-Anilino-1-naphthalenesulfonic acid (ANS) fluorescence spectra of human reticulocalbin 1 (hRCN1). (A) Effect of divalent metal cations on ANS fluorescence. The protein solution consisted of 10 μM hRCN1, 100 μM ANS, 5 mM MOPS-KOH (pH 7.5), 50 mM KCl and 2 mM of EDTA, CaCl₂, SrCl₂, MgCl₂, or BaCl₂ (indicated as apo, Ca²⁺, Sr²⁺, Mg²⁺ or Ba²⁺, respectively). The spectrum of the solution without hRCN1 is indicated as ANS. The excitation wavelength was 370 nm and the emission was recorded from 400 to 600 nm. (B) Effect of various Ca²⁺ concentrations on ANS fluorescence. The protein solution consisted of 10 μM hRCN1, 100 μM ANS, 5 mM MOPS-KOH (pH 7.5), 50 mM KCl, and various concentrations of CaCl₂ from 0 to 10 mM. The spectrum of the solution without hRCN1 is indicated as ANS.

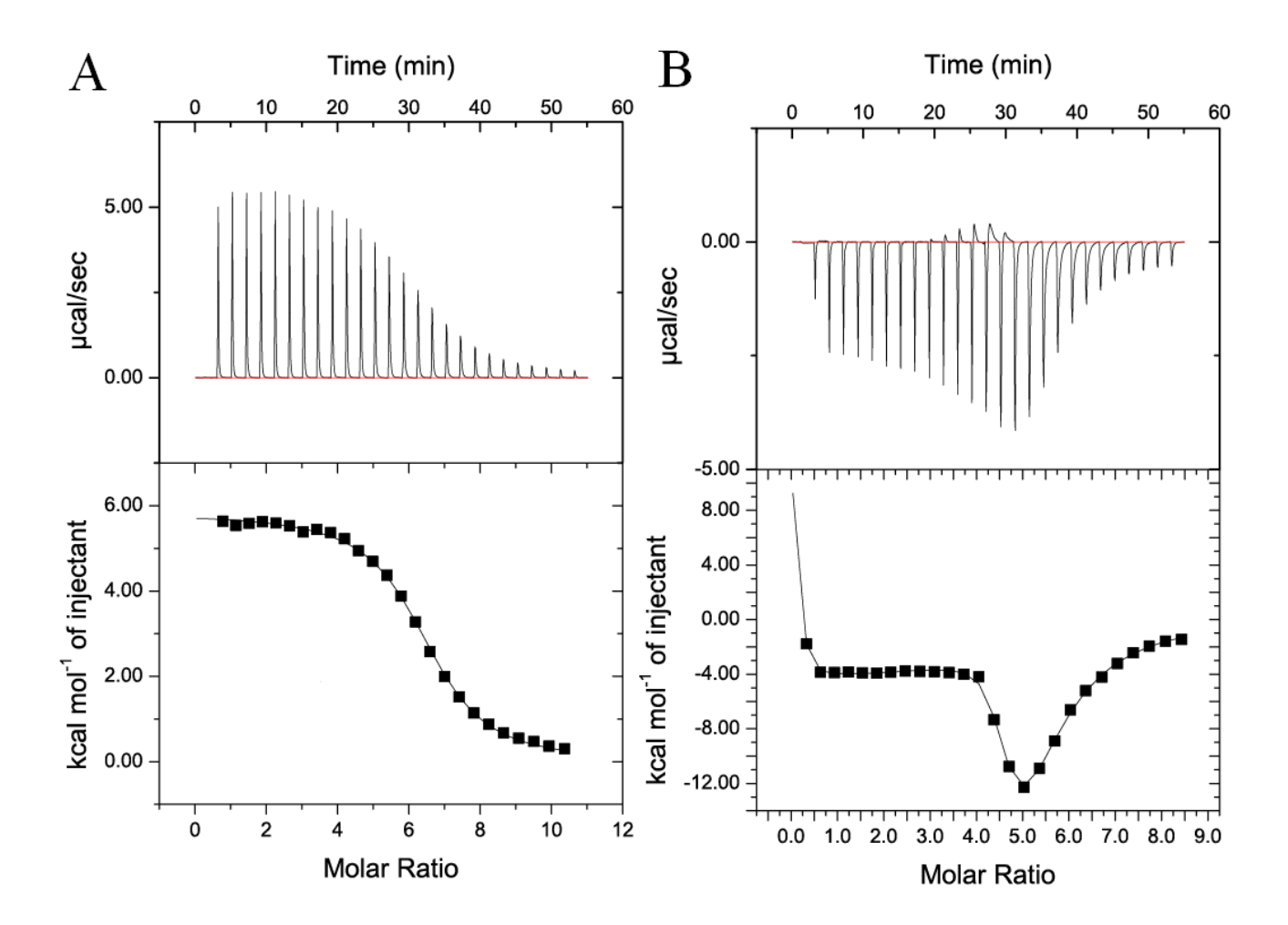
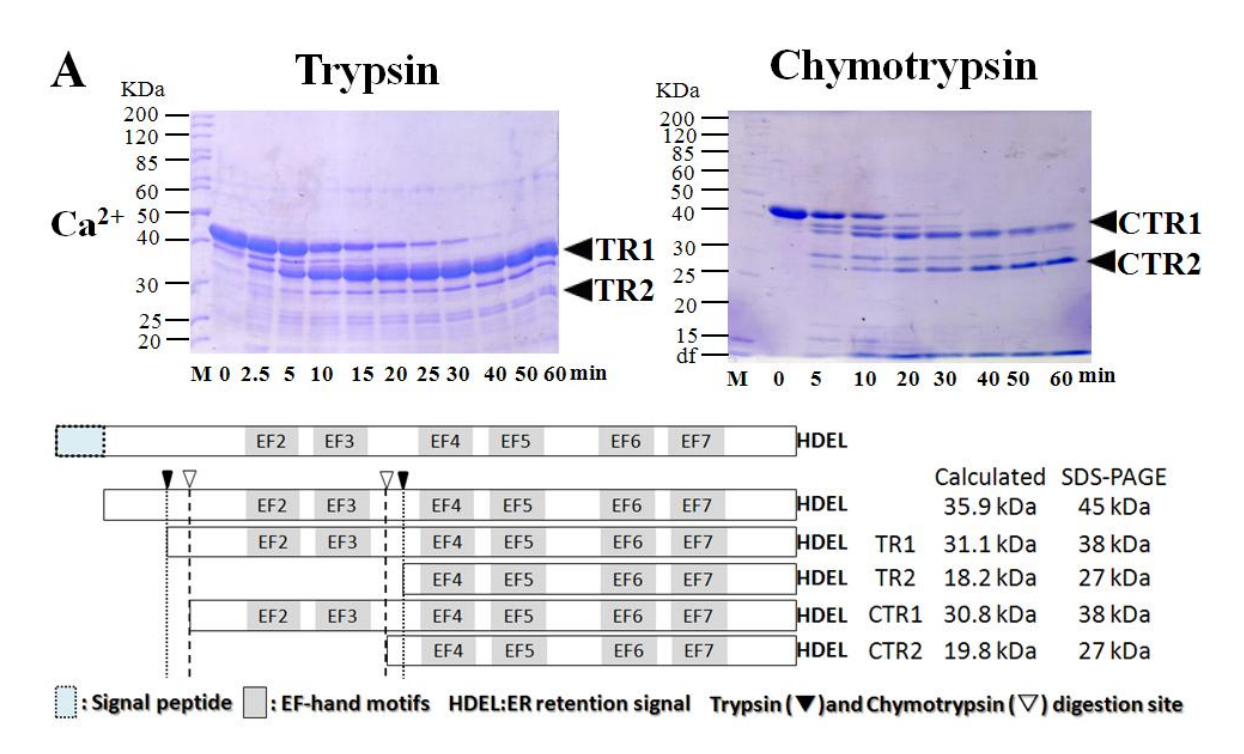


Figure II-6 Microcalorimetric titration of hRCN1 with Mg²⁺ **and Ca**²⁺. (A) For Mg²⁺ titration, the protein solution contained 10 mM Pipes-NaOH (pH 6.8) and 100 mM NaCl. The sample cell was filled with 204 μL of 122 μM hRCN1 solution and 26 consecutive 1.5 μL aliquots of the outer dialysate containing 6 mM MgCl₂ were injected at 120 s intervals. (B) For Ca²⁺-titration, the protein solution was the same as that for Mg²⁺ titration experiment and the sample cell was filled with 204 μL of 100 μM hRCN1 solution and 26 consecutive 1.5 μL aliquots of the outer dialysate containing 4 mM CaCl₂ were injected at 120 s intervals.



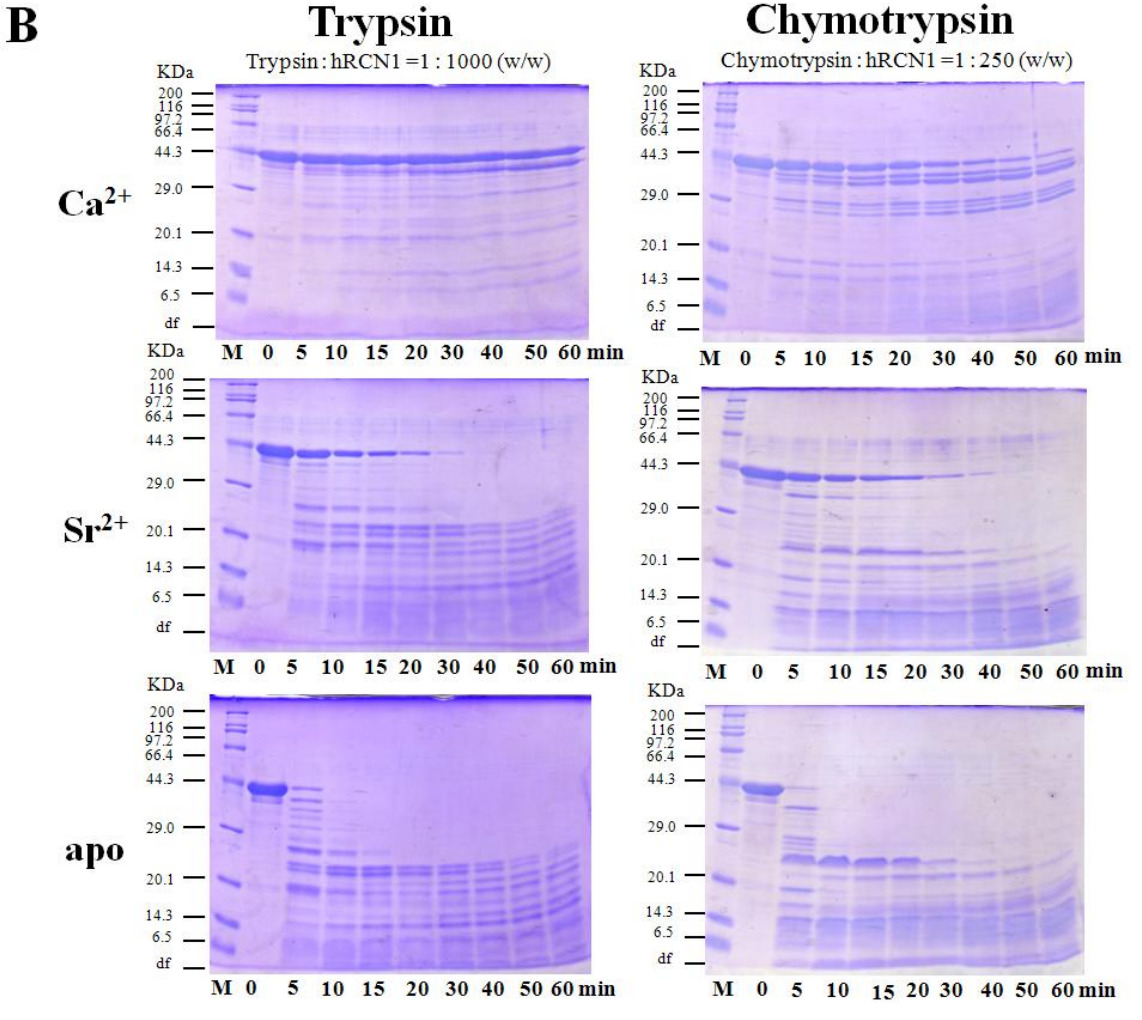


Figure II-7 Limited proteolysis of human reticulocalbin 1 (RCN1) with trypsin and chymotrypsin. (A) Time course analysis of tryptic and chymtryptic digestion of Ca²⁺-bound hRCN1 at the enzyme/substrate ratio of 1/100 (w/w) by SDS-PAGE. hRCN1 digested with trypsin (left panel) and chymotrypsin (right panel). The fragment bands subjected to further purification and amino acid sequencing are indicated by black arrow heads with TR1 and TR2 for tryptic fragments and CTR1 and CTR2 for chymotryptic fragments. M: molecular mass standards. Molecular masses are shown on the left. The gels were stained with Coomassie brilliant blue. Schematic representations of digestion sites related with the positions of EF-hand motifs on hRCN1 are shown at the bottom. The calculated and experimentally obtained molecular masses are shown on the right of each corresponding fragment. (B) Limited degradation differences of hRCN1 with various metal ions. Time course analysis of tryptic and chymtryptic digestion of metal cation or EDTA loaded-hRCN1 by SDS-PAGE. These panels show the SDS gels of Ca²⁺, Sr²⁺ and EDTA-loaded hRCN1 digested with 1/1000 (w/w) trypsin (left panel) and 1/250 (w/w) chymotrypsin (right panel).

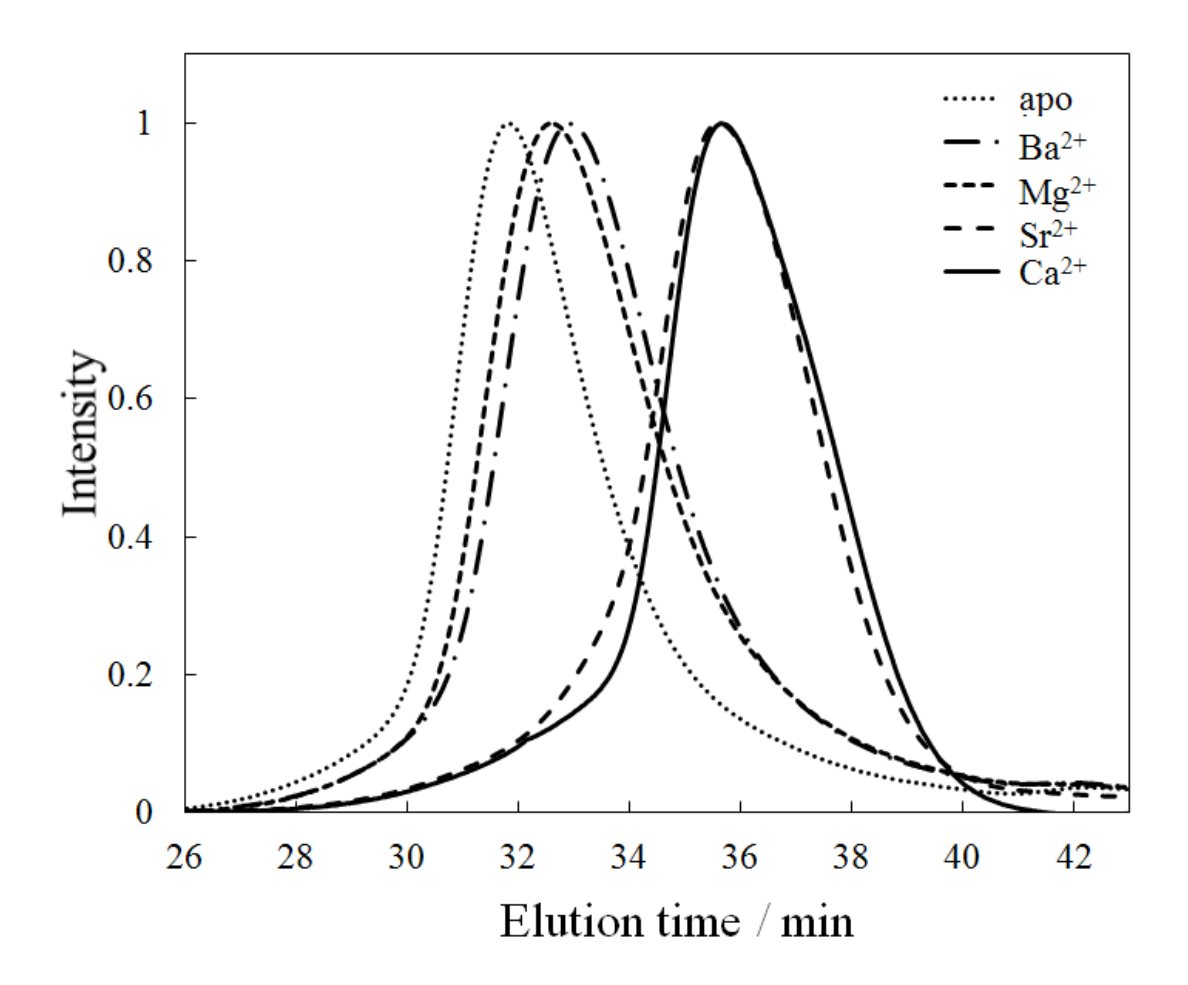


Figure II-8 Gel filtration of apo and Ca²⁺-bound human reticulocalbin 1 (hRCN1).

hRCN1 was chromatographed on a Superdex 200 column at a flow rate of 0.4 mL/min. Protein was detected at 230 nm. Relative absorbance is shown by adjusting the peak absorbances to 1. The elution buffer was 25 mM Tris-HCl (pH 7.5) and 150 mM NaCl for analysis of apo hRCN1, and 2 mM BaCl₂, MgCl₂, SrCl₂ or CaCl₂ was added to both the hRCN1 solution and the elution buffer for analysis of Ba²⁺, Mg²⁺, Sr²⁺ or Ca²⁺-loaded hRCN1.

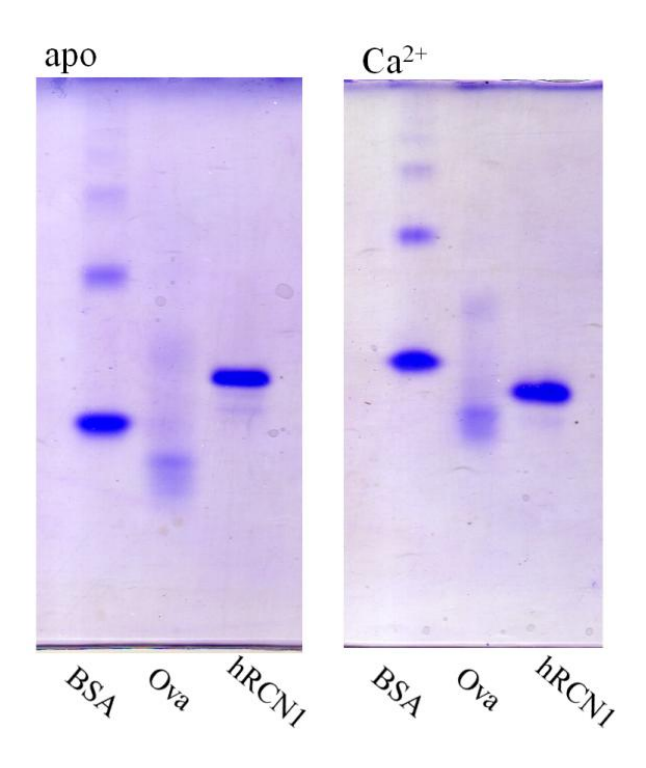
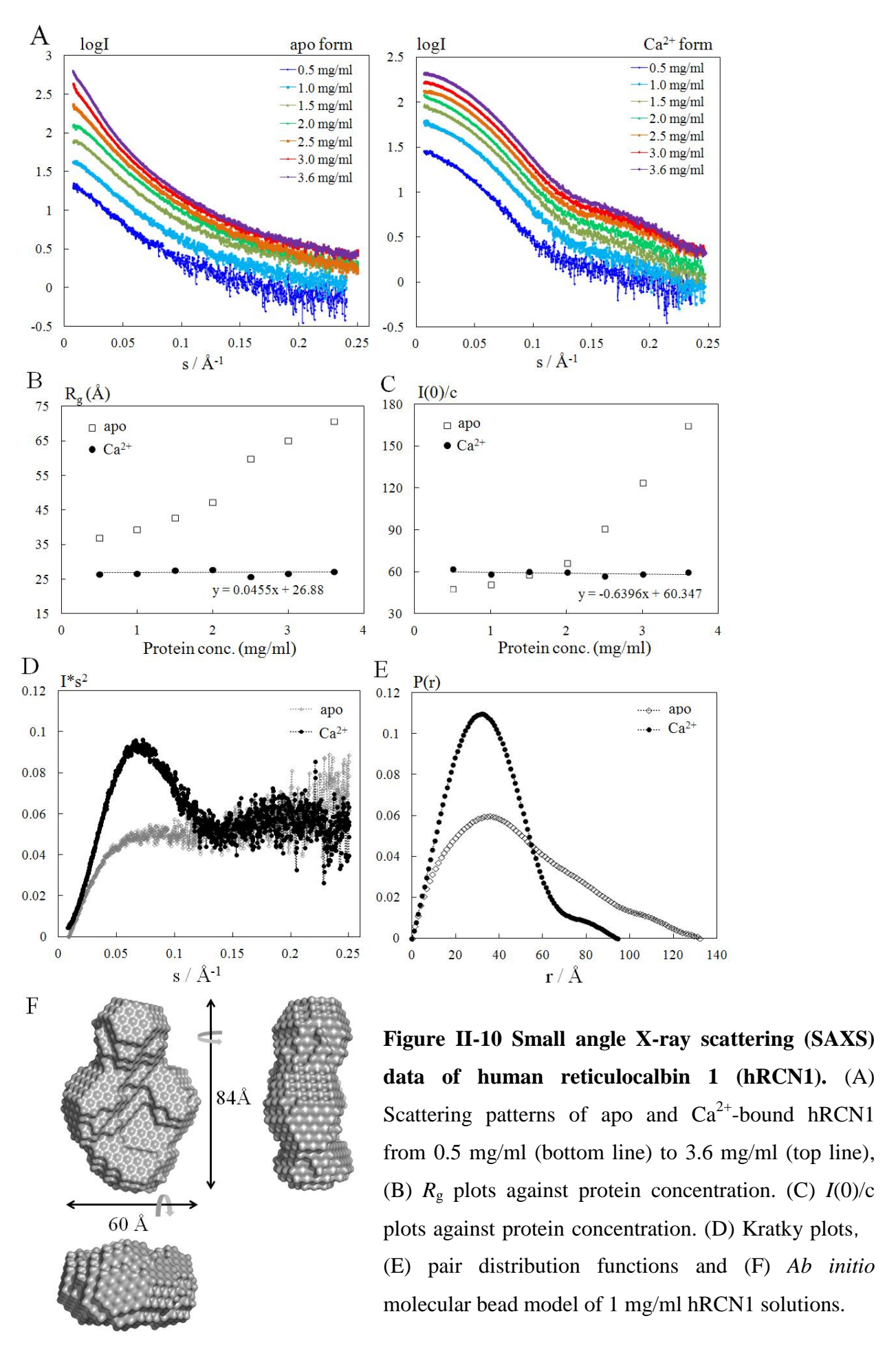


Figure II-9 Native-PAGE of human reticulocalbin 1 (hRCN1). Native-PAGE was performed on 10 % (w/v) separating gels. Protein samples were 1 mg/ml solutions of hRCN1, BSA and ovalbumin in 25 mM HEPES-KOH (pH7.5) and 100 mM KCl. BSA and ovalbumin (Ova) were used as standard proteins to compare mobilities of hRCN1 in the presence and absence of Ca²⁺. Gels were run in 100 mM Tris-HCl (pH7.8) for anode and 25 mM Tris and 192 mM Glycine for cathode at 15 mA. 0.5 M EDTA or 1 M CaCl₂ was added to both anode and cathode running buffers to give the final concentration of EDTA and Ca²⁺ at 4 mM before beginning the runs in the absence or presence of Ca²⁺, respectively. The gels were stained with Coomassie brilliant blue.



CHAPTER III

Development and evaluation of a new SAXS system for biological samples

Summary

SAXS is a well-known technique for studying the size and shape of particles in solution. More recently SAXS has been recognized as a complementary tool for extracting structural information from biological systems where X-ray crystallographic methods have failed. SAXS is also considered a useful tool to study behavior of a macromolecule under varied chemical conditions.

However, to get reliable data from SAXS, the sample should be monodispersed in the solution at low concentration. Conventional home laboratory systems require two or more hours per exposure due to the weak signal from the sample. Access to synchrotron facilities is also very limited, thus there is a demand for a fast system for the home laboratory.

Here I introduce the first commercial system specifically designed for high-throughput solution scattering experiments with macromolecules, the BioSAXS-1000. Comprised of specially designed focusing optics with Kratky collimation, the BioSAXS-1000 system eliminates smearing issues common to traditional Kratky cameras and provides sufficient flux for measuring scattering data for low concentration biological samples. This paper will summarize data collection and analyses for data collected on the BioSAXS-1000 for several protein samples, including *ab initio* protein envelopes.

1. Introduction

SAXS is a well-known technique for studying the size and the shape of particles in solution. More recently, SAXS has undergone a resurgence as a useful tool to study biological samples.

X-ray crystallography is a fundamental technique for obtaining atomic resolution structural information for macromolecules. However, the requirement for diffraction quality crystals often limits its efficacy for studying protein complexes or systems with inherent structural disorder. In cases where crystallographic methods have failed, SAXS provides a complementary tool for extracting structural information from biological systems (Hura *et al.* 2009). In particular, SAXS proves ideal for studying partially disordered macromolecules, for monitoring structural changes in response to environmental perturbations, and for monitoring conformational changes due to ligand binding. It is also a useful tool for probing the crystallization slot".

Here I introduce the system specifically designed for high-throughput solution scattering experiments for macromolecules in solution, the BioSAXS-1000. Comprised of specially designed focusing optics and a Kratky block, the BioSAXS-1000 system eliminates smearing issues common to traditional Kratky cameras (JIANG 2000). The system features a high sensitivity pixel array detector and intuitive data collection software that includes full automation of the Kratky alignment hardware. Together, these features of the BioSAXS-1000 system allow for synchrotron-quality SAXS data from a home laboratory source.

2. Development of the system

(a) Optics

Conventional SAXS systems use the three pinhole design, employing a monochromator or Confocal Multi Layer optic (CMF) as a beam conditioner. Advances in X-ray optics over the last two decades have offered great improvement in the quality of X-ray beams from home labs in terms of flux and spectral purity. The advent of CMF optics during the 1990s provided significant increases in X-ray flux for home laboratory systems (VERMAN *et al.* 2000). These advances have greatly enabled the expansion of both X-ray crystallographic and SAXS experiments in home laboratories.

A three pinhole system is ideal for measuring anisotropic samples but the requisite parallel beam has relatively low flux, making it difficult to measure weakly scattering samples, especially at low concentration. Another collimation system uses a Kratky block with a line-shaped beam. This design produces much higher flux but suffers from a distortion to the image data known as smearing.

Here I introduce a new system that consists of a specially designed focusing CMF, with the focus is on the detector surface and a Kratky block. The Kratky block is designed such that the bottom surface of one block is parallel to the top surface of the other, and the blocks are rotatable about the beam around a pivot. The advantage of this design is that the beam intensity distribution at the detector position is independent of the collimation produced by the block.

Furthermore, Kratky cameras significantly outperform pinhole cameras for experiments on large particles, as in the case of macromolecules. Figure III-2 shows a schematic of the flux reduction in the tightly collimated pinhole system, limiting the

beam "seen" by the solution sample. This decrease in intensity directly translates to a reduction in scattering signal at the detector.

A unique feature of the Kratky camera is the ability to change the q value in cases where low q measurements are required. Specifically, a Kratky block limits the converging beam by virtue of rotation and translations. As illustrated Figure III-3, in the "high q_{min}" mode, the Kratky block does not occlude the beam. At the sample position, the beam size is more quadrate. When the Kratky block is rotated to occlude the X-ray beam, the beam shape becomes more rectangular. These changes to the overall shape of the beam at the sample have a direct impact on the accessible q_{min} for data collection. Thus, the Kratky camera is ideal for measuring large particles, as in the case of macromolecules and macromolecular complexes. Though changes to the Kratky angle reduce the flux at the sample position, Kratky cameras produce greater flux in "low q" mode than pinhole cameras when installed on an identical source.

(b) Sample holder

The sample holder has 3 positions for sample capillary cells and one for a standard sample for calibration of q and the beam center. Liquid samples can be injected using Pipetman® or a syringe; a typical amount is $30 \, \mu l$.

The three samples are automatically measured using motorized X Y movements. This sample holder also has temperature control, with a range of 4 °C to 90 °C when water is used as the coolant.

During the exchange of a sample, the entire sample holder assembly can be pulled to the outside of the instrument as show in Figure III-4 and an operator can easily load a freshly charged capillary cell, then push it back to the inside.

(c)Beam Stop and Detector

The beam stop has a built in pin-diode and the continuously measured intensity is automatically saved to the log file. Although the laboratory source does not show intensity fluctuations, the transmission factor can be calculated and used for the scaling of sample data and buffer subtraction.

For the detector, the most advanced pixel array detector is used with a dynamic range of more than 10^6 photon counting capability. Both lower q, high intensity data and high q, low intensity can be measured concurrently. The maximum q value is better than $0.7 \ \text{Å}^{-1}$.

3. Results

Scattering data were collected for glucose isomerase (GI) on the BioSAXS-1000 and averaged one dimensionally using SAXSGUI then processed using the ATSAS2.1 software package (PETOUKHOV *et al.* 2007). Followed by buffer subtraction with PRIMUS (PETOUKHOV *et al.* 2007). Output from PRIMUS was used to create PDDFs (Particle Distance Distribution Function), with GNOM (PETOUKHOV *et al.* 2007), to a q_{max} of ~0.3 Å⁻¹ ("medium q" data) and 0.64 Å⁻¹ ("high q" data), respectively. Fifteen *ab initio* envelopes were generated with DAMMIF (PETOUKHOV *et al.* 2007) and GASBOR (PETOUKHOV *et al.* 2007) for the ~0.3 Å⁻¹ and 0.64 Å⁻¹ data, respectively. The fifteen envelopes were superimposed and averaged for each data set with DAMAVER (PETOUKHOV *et al.* 2007).

As shown Figure III-5 the envelopes determined with high q data are more comparable to the size of the protein molecule and exhibit greater faithfulness to the surface of the protein compared to the envelope determined using "medium q" data.

The Figure III-6 shows several protein envelopes obtained using the BioSAXS-1000. Data were processed using the same method as described above.

4. Conclusion

In this paper I present a new instrument, the BioSAXS-1000, which provides complementary structural information to X-ray crystallography and NMR. The system utilizes a motorized Kratky block for adjustments to q_{min} for measurement of large particles, such as macromolecular complexes and viral particles. The BioSAXS-1000 is the highest brilliance SAXS instrument available on a home source and provides a powerful platform for maximizing the experimental workflow for structural biology laboratories.



Figure III-1 The BioSAXS-1000 System

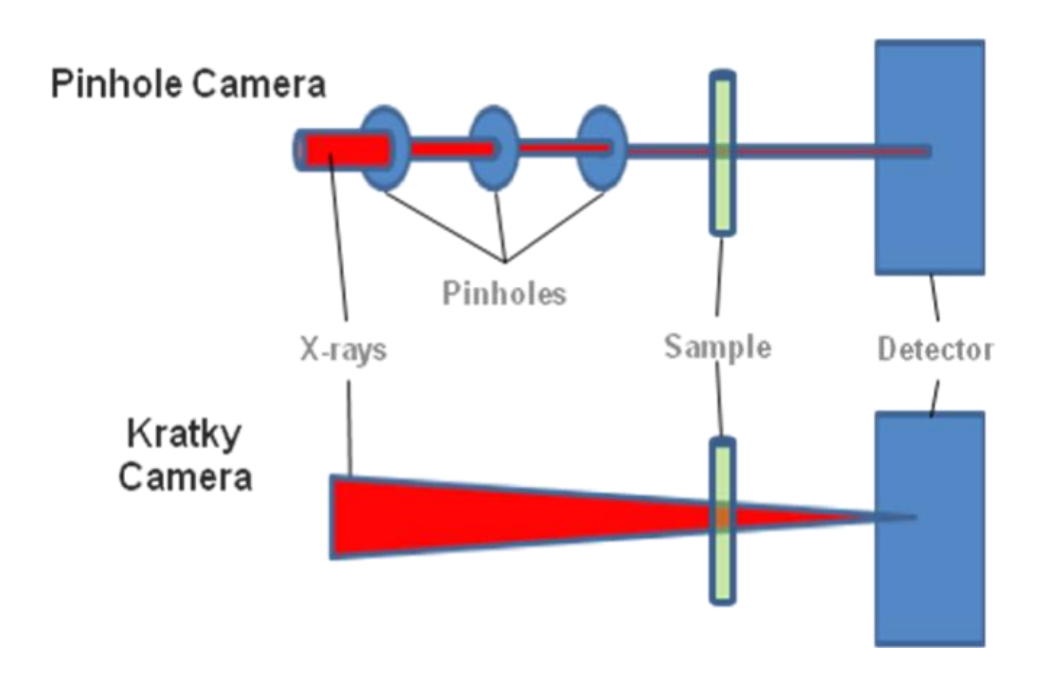


Figure III-2: Schematic comparison of pinhole and Kratky camera geometries

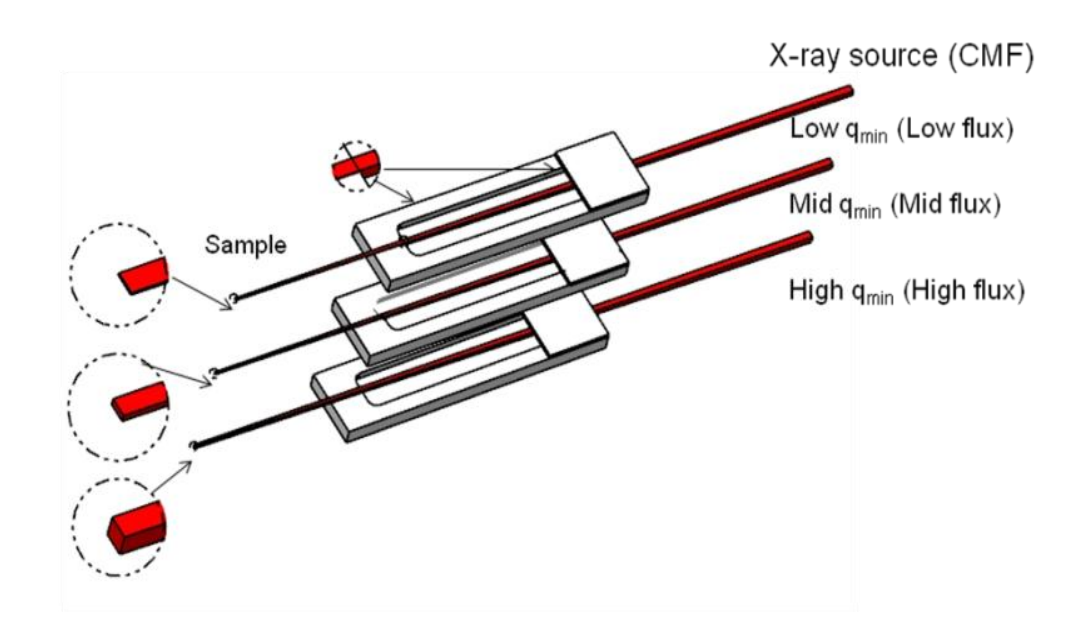


Figure III-3: Schematic of beam shape changes with increasing Kratky block angle

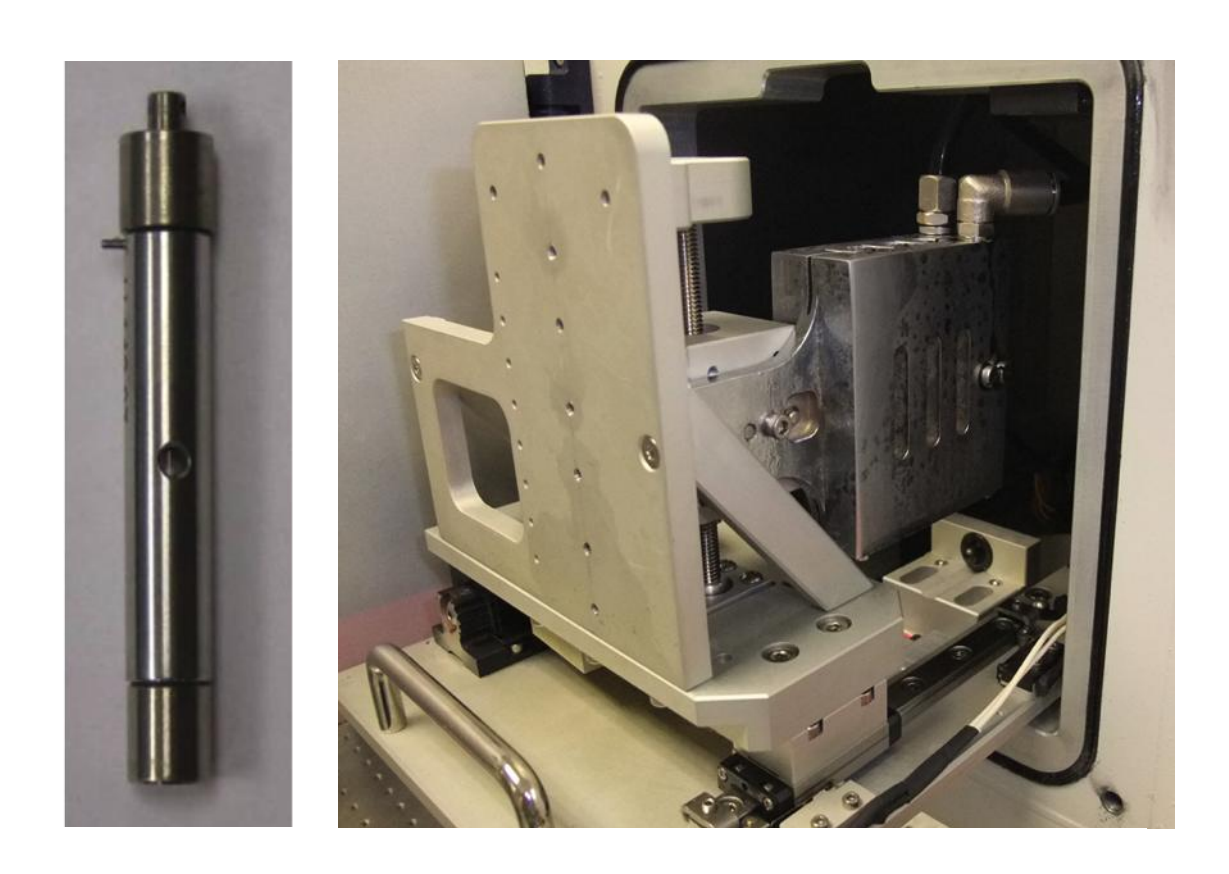


Figure III-4: Photograph of the capillary cell and sample stage with temperature control

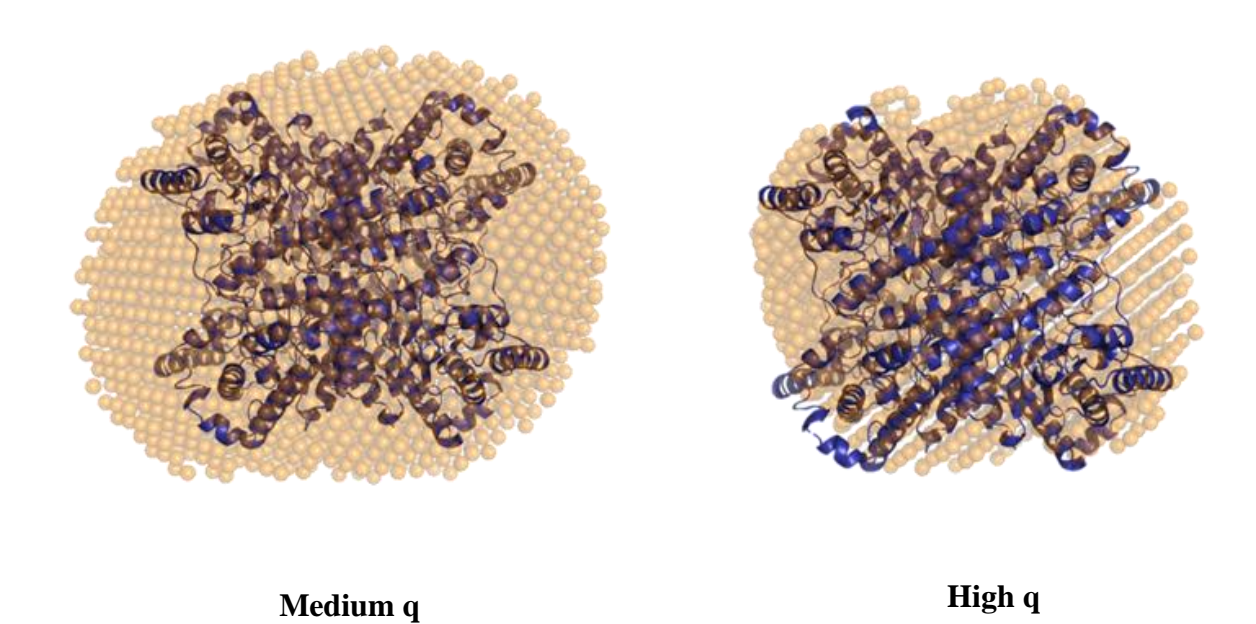


Figure III-5 Average envelopes 5 mg/ml Glucose Isomerase determined from 'medium q' and 'high q' Rigaku FR-E+ X-ray generator 45KV, 55 mA, Exposure 30 min data

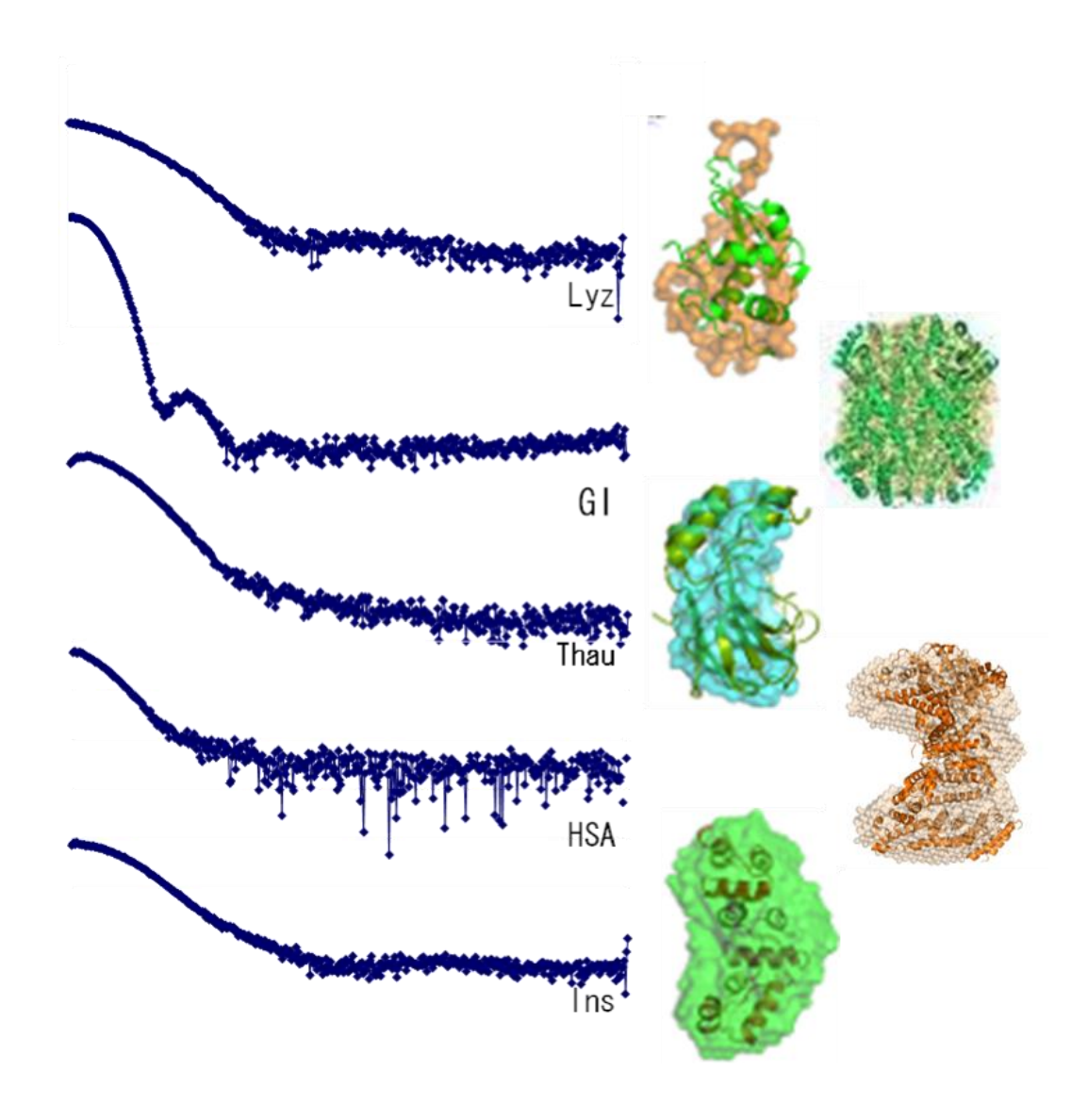


Figure III-6: SAXS analysis for several proteins: lysozyme (Lyz), glucose isomerase (GI), thaumatin (Thau), human serum albumin (HSA), and insulin (Ins)

AKNOWLEDGEMENTS

I would like to thank late Professor Minoru Nakano and Associate Professor Naoto Yonezawa for their valuable advice throughout the course of this research.

I thank Dr. Masayuki Nara of Tokyo Medical and Dental University, Dr. Masaru Tanokura, Dr, Koji Nagata, Dr. Yusuke Kato, Dr. Fumiaki Yumoto, Dr. Yoriko Sawano Dr. Takuya Miyakawa and Dr. Fabiana L. Imai of Tokyo University and Dr. Akira Sakamoto of Saitama University for their support for my research.

I would like to extend my special thanks to Dr. Mark Haley of Chiba University, Dr. Katsunari Sasaki, Dr. Joseph Ferrara, and Dr. Angela Criswell of Rigaku Americas cooperation very much for the great support for all SAXS experiment. I also thank Dr. Yamano and Dr. Matsumoto (Rigaku) for supports and advices for SAXS measurements.

Finally, I am thankful to the member of my laboratory at Chiba University for their great support.

REFERENCES

- ARRONDO, J. L., A. MUGA, J. CASTRESANA and F. M. GONI, 1993 Quantitative studies of the structure of proteins in solution by Fourier-transform infrared spectroscopy. Prog Biophys Mol Biol **59**: 23-56.
- BABU, Y. S., C. E. BUGG and W. J. COOK, 1988 Structure of calmodulin refined at 2.2 A resolution. J Mol Biol **204**: 191-204.
- BABU, Y. S., J. S. SACK, T. J. GREENHOUGH, C. E. BUGG, A. R. MEANS *et al.*, 1985

 Three-dimensional structure of calmodulin. Nature **315**: 37-40.
- BARTH, A., 2000 The infrared absorption of amino acid side chains. Prog Biophys Mol Biol **74:** 141-173.
- BARTH, A., 2007 Infrared spectroscopy of proteins. Biochim Biophys Acta 1767: 1073-1101.
- BARTH, A., and C. ZSCHERP, 2002 What vibrations tell us about proteins. Q Rev Biophys **35**: 369-430.
- BAYLEY, P. M., and S. R. MARTIN, 1992 The alpha-helical content of calmodulin is increased by solution conditions favouring protein crystallisation. Biochim Biophys Acta 1160: 16-21.
- BERRIDGE, M. J., M. D. BOOTMAN and P. LIPP, 1998 Calcium--a life and death signal.

 Nature **395**: 645-648.
- BERRIDGE, M. J., P. LIPP and M. D. BOOTMAN, 2000 The versatility and universality of calcium signalling. Nat Rev Mol Cell Biol 1: 11-21.
- CHATTOPADHYAYA, R., W. E. MEADOR, A. R. MEANS and F. A. QUIOCHO, 1992 Calmodulin structure refined at 1.7 A resolution. J Mol Biol 228: 1177-1192.

- CHEN, Y. H., J. T. YANG and H. M. MARTINEZ, 1972 Determination of the secondary structures of proteins by circular dichroism and optical rotatory dispersion. Biochemistry 11: 4120-4131.
- COOPER, C. R., B. GRAVES, F. PRUITT, H. CHAIB, J. E. LYNCH *et al.*, 2008 Novel surface expression of reticulocalbin 1 on bone endothelial cells and human prostate cancer cells is regulated by TNF-alpha. J Cell Biochem **104**: 2298-2309.
- DEACON, G. B., and R. J. PHILLIPS, 1980 Relationships between the carbon-oxygen stretching frequencies of carboxylate complexes and the type of carboxylate coordination. Coord. Chem. Rev. **33**: 227–250.
- DONIACH, S., 2001 Changes in biomolecular conformation seen by small angle X-ray scattering. Chem Rev **101:** 1763-1778.
- FABIAN, H., T. YUAN, H. J. VOGEL and H. H. MANTSCH, 1996 Comparative analysis of the amino- and carboxy-terminal domains of calmodulin by Fourier transform infrared spectroscopy. Eur Biophys J **24**: 195-201.
- FRANKE, D., and D. I. SVERGUN, 2009 DAMMIF, a program for rapidab-initioshape determination in small-angle scattering. Journal of Applied Crystallography **42**: 342-346.
- GIFFORD, J. L., M. P. WALSH and H. J. VOGEL, 2007 Structures and metal-ion-binding properties of the Ca²⁺-binding helix-loop-helix EF-hand motifs. Biochem J **405**: 199-221.
- GRABAREK, Z., 2005 Structure of a trapped intermediate of calmodulin: calcium regulation of EF-hand proteins from a new perspective. J Mol Biol **346**: 1351-1366.

- GRABAREK, Z., 2006 Structural basis for diversity of the EF-hand calcium-binding proteins. J Mol Biol **359**: 509-525.
- GRABAREK, Z., 2011 Insights into modulation of calcium signaling by magnesium in calmodulin, troponin C and related EF-hand proteins. Biochim Biophys Acta **1813**: 913-921.
- GREENFIELD, N., and G. D. FASMAN, 1969 Computed circular dichroism spectra for the evaluation of protein conformation. Biochemistry **8:** 4108-4116.
- HONORE, B., 2009 The rapidly expanding CREC protein family: members, localization, function, and role in disease. Bioessays **31:** 262-277.
- HONORE, B., and H. VORUM, 2000 The CREC family, a novel family of multiple EF-hand, low-affinity Ca²⁺-binding proteins localised to the secretory pathway of mammalian cells. FEBS Lett **466:** 11-18.
- HUANG, H., H. ISHIDA and H. J. VOGEL, 2010 The solution structure of the Mg²⁺ form of soybean calmodulin isoform 4 reveals unique features of plant calmodulins in resting cells. Protein Sci **19:** 475-485.
- HURA, G. L., A. L. MENON, M. HAMMEL, R. P. POOLE 2ND, S. E. TSUTAKAWA *et al.*, 2009 Robust, high-throughput solution structural analyses by small angle X-ray scattering (SAXS). Nature Methods **6:** 606-612.
- ISHIDA, H., H. HUANG, A. P. YAMNIUK, Y. TAKAYA and H. J. VOGEL, 2008 The solution structures of two soybean calmodulin isoforms provide a structural basis for their selective target activation properties. J Biol Chem 283: 14619-14628.
- JACKSON, M., P. I. HARIS and D. CHAPMAN, 1991 Fourier transform infrared spectroscopic studies of Ca²⁺-binding proteins. Biochemistry **30**: 9681-9686.

- JIANG, L., 2006 Two-dimensional small angle X-ray scattering camera. US patent: 7, 734, 001 B2 (worldwide patents pending).
- KARITA, E., H. YAMAKAWA, I. MITSUHARA, K. KUCHITSU and Y. OHASHI, 2004 Three types of tobacco calmodulins characteristically activate plant NAD kinase at different Ca²⁺ concentrations and pHs. Plant Cell Physiol **45**: 1371-1379.
- KONAREV, P. V., M. V. PETOUKHOV, V. V. VOLKOV and D. I. SVERGUN, 2006 ATSAS2.1, a program package for small-angle scattering data analysis. Journal of Applied Crystallography **39:** 277-286.
- KONAREV, P. V., V. V. VOLKOV, A. V. SOKOLOVA, M. H. J. KOCH and D. I. SVERGUN, 2003 PRIMUS: aWindows PC-based system for small-angle scattering data analysis. Journal of Applied Crystallography **36:** 1127-1283.
- Kong, J., and S. Yu, 2007 Fourier transform infrared spectroscopic analysis of protein secondary structures. Acta Biochim Biophys Sin (Shanghai) **39:** 549-559.
- KUBONIWA, H., N. TJANDRA, S. GRZESIEK, H. REN, C. B. KLEE *et al.*, 1995 Solution structure of calcium-free calmodulin. Nat Struct Biol **2:** 768-776.
- LAEMMLI, U. K., 1970 Cleavage of structural proteins during the assembly of the head of bacteriophage T4. Nature **227**: 680-685.
- LEE, S. H., J. C. KIM, M. S. LEE, W. D. HEO, H. Y. SEO *et al.*, 1995 Identification of a novel divergent calmodulin isoform from soybean which has differential ability to activate calmodulin-dependent enzymes. J Biol Chem **270**: 21806-21812.
- MELDOLESI, J., and T. POZZAN, 1998 The endoplasmic reticulum Ca²⁺ store: a view from the lumen. Trends Biochem Sci **23:** 10-14.
- MIZUGUCHI, M., M. NARA, K. KAWANO and K. NITTA, 1997a FT-IR study of the Ca²⁺-binding to bovine alpha-lactalbumin. Relationships between the type of

- coordination and characteristics of the bands due to the Asp COO⁻ groups in the Ca²⁺-binding site. FEBS Lett **417:** 153-156.
- MIZUGUCHI, M., M. NARA, Y. KE, K. KAWANO, T. HIRAOKI *et al.*, 1997b Fourier-transform infrared spectroscopic studies on the coordination of the side-chain COO⁻ groups to Ca²⁺ in equine lysozyme. Eur J Biochem **250**: 72-76.
- NARA, M., H. MORII and M. TANOKURA, 2013 Infrared study of synthetic peptide analogues of the calcium-binding site III of troponin C: The role of helix F of an EF-hand motif. Biopolymers **99:** 342-347.
- NARA, M., and M. TANOKURA, 2008 Infrared spectroscopic study of the metal-coordination structures of calcium-binding proteins. Biochem Biophys Res Commun **369**: 225-239.
- NARA, M., M. TANOKURA, T. YAMAMOTO and M. TASUMI, 1995 A comparative study of the binding effects of Mg²⁺, Ca²⁺, Sr²⁺, and Cd²⁺ on calmodulin by fourier-transform infrared spectroscopy. Biospectroscopy **1:** 47.
- NARA, M., M. TASUMI, M. TANOKURA, T. HIRAOKI, M. YAZAWA *et al.*, 1994 Infrared studies of interaction between metal ions and Ca²⁺-binding proteins. Marker bands for identifying the types of coordination of the side-chain COO⁻ groups to metal ions in pike parvalbumin (pI = 4.10). FEBS Lett **349**: 84-88.
- NARA, M., H. TORII and M. TASUMI, 1996 Correlation between the Vibrational Frequencies of the Carboxylate Group and the Types of Its Coordination to a Metal Ion: An ab Initio Molecular Orbital Study. J. Phys. Chem. **100:** 19812.
- NARA, M., F. YUMOTO, H. KAGI and M. TANOKURA, 2008 Infrared spectroscopic study of the binding of divalent cations to Akazara scallop troponin C: the effect of the methylene side chain of glutamate residue. Biopolymers **89:** 595-599.

- NARA, M., F. YUMOTO, K. NAGATA, M. TANOKURA, H. KAGI *et al.*, 2004 Fourier transform infrared spectroscopic study on the binding of Mg²⁺ to a mutant Akazara scallop troponin C (E142Q). Biopolymers **74:** 77-81.
- OZAWA, M., 1995 Cloning of a human homologue of mouse reticulocalbin reveals conservation of structural domains in the novel endoplasmic reticulum resident Ca²⁺-binding protein with multiple EF-hand motifs. J Biochem **117**: 1113-1119.
- OZAWA, M., and T. MURAMATSU, 1993 Reticulocalbin, a novel endoplasmic reticulum resident Ca²⁺-binding protein with multiple EF-hand motifs and a carboxyl-terminal HDEL sequence. J Biol Chem **268**: 699-705.
- OZAWA, T., M. FUKUDA, M. NARA, A. NAKAMURA, Y. KOMINE *et al.*, 2000 How can Ca²⁺ selectively activate recoverin in the presence of Mg²⁺? Surface plasmon resonance and FT-IR spectroscopic studies. Biochemistry **39**: 14495-14503.
- PACE, C. N., F. VAJDOS, L. FEE, G. GRIMSLEY and T. GRAY, 1995 How to measure and predict the molar absorption coefficient of a protein. Protein Sci 4: 2411-2423.
- Petoukhov, M. V., P. V. Konarev, A. G. Kikhney and D. I. Svergun, 2007 ATSAS 2.1 towards automated and websupported small-angle scattering data analysis. Journal of Applied Crystallography **40:** s223-s228.
- QUEIROZ, J. A., C. T. TOMAZ and J. M. CABRAL, 2001 Hydrophobic interaction chromatography of proteins. J Biotechnol 87: 143-159.
- ROMANI, A. M., 2011 Cellular magnesium homeostasis. Arch Biochem Biophys **512**: 1-23.
- ROYER, C. A., 2006 Probing protein folding and conformational transitions with fluorescence. Chem Rev **106:** 1769-1784.

- SENGUEN, F. T., and Z. GRABAREK, 2012 X-ray Structures of Magnesium and Manganese Complexes with the N-Terminal Domain of Calmodulin: Insights into the Mechanism and Specificity of Metal Ion Binding to an EF-Hand. Biochemistry.
- SHANNON, R. D., 1976 Revised effective ionic radii and systematic studies of interatomic distances in halides and chalcogenides. Acta Crystallographica Section A 32.
- STRYNADKA, N. C., and M. N. JAMES, 1989 Crystal structures of the helix-loop-helix calcium-binding proteins. Annu Rev Biochem **58:** 951-998.
- SVERGUN, D. I., 1992 Determination of the regularization parameter in indirect-transform methods using perceptual criteria. Journal of Applied Crystallography 25: 495-503.
- TACHIKUI, H., A. F. NAVET and M. OZAWA, 1997 Identification of the Ca²⁺-binding domains in reticulocalbin, an endoplasmic reticulum resident Ca²⁺-binding protein with multiple EF-hand motifs. J Biochem **121**: 145-149.
- TAKEZAWA, D., Z. H. LIU, G. AN and B. W. POOVAIAH, 1995 Calmodulin gene family in potato: developmental and touch-induced expression of the mRNA encoding a novel isoform. Plant Mol Biol 27: 693-703.
- TREWHELLA, J., W. K. LIDDLE, D. B. HEIDORN and N. STRYNADKA, 1989 Calmodulin and troponin C structures studied by Fourier transform infrared spectroscopy: effects of Ca²⁺ and Mg²⁺ binding. Biochemistry **28:** 1294-1301.
- TSUKUMO, Y., S. TSUKAHARA, S. SAITO, T. TSURUO and A. TOMIDA, 2009 A novel endoplasmic reticulum export signal: proline at the +2-position from the signal peptide cleavage site. J Biol Chem **284**: 27500-27510.

- VERMAN, B, L. JIANG, B. KIM, R. SMITH, and N. GRUPIDO, 2000 Confocal Graded d-spacing multilayer beam conditioning optics. Advance in X-ray Analysis 42: 321-332.
- VOLKOVA, V. V., and D. I. SVERGUN, 2003 Uniqueness of ab initio shape determination in small-angle scattering. Journal of Applied Crystallography **36:** 860-864.
- VORUM, H., X. LIU, P. MADSEN, H. H. RASMUSSEN and B. HONORE, 1998 Molecular cloning of a cDNA encoding human calumenin, expression in Escherichia coli and analysis of its Ca²⁺-binding activity. Biochim Biophys Acta **1386**: 121-131.
- YAMAKAWA, H., S. KATOU, S. SEO, I. MITSUHARA, H. KAMADA *et al.*, 2004 Plant MAPK phosphatase interacts with calmodulins. J Biol Chem **279**: 928-936.
- YAMAKAWA, H., I. MITSUHARA, N. ITO, S. SEO, H. KAMADA *et al.*, 2001

 Transcriptionally and post-transcriptionally regulated response of 13 calmodulin genes to tobacco mosaic virus-induced cell death and wounding in tobacco plant.

 Eur J Biochem **268**: 3916-3929.
- YOSHIDA, Y., T. YAMASHITA, K. NAGANO, S. IMAI, H. NABESHI *et al.*, 2011 Limited expression of reticulocalbin-1 in lymphatic endothelial cells in lung tumor but not in normal lung. Biochem Biophys Res Commun **405**: 610-614.
- YUMOTO, F., M. NARA, H. KAGI, W. IWASAKI, T. OJIMA *et al.*, 2001 Coordination structures of Ca²⁺ and Mg²⁺ in Akazara scallop troponin C in solution. FTIR spectroscopy of side-chain COO- groups. Eur J Biochem **268**: 6284-6290.
- YUN, C. H., J. BAI, D. Y. SUN, D. F. CUI, W. R. CHANG *et al.*, 2004 Structure of potato calmodulin PCM6: the first report of the three-dimensional structure of a plant calmodulin. Acta Crystallogr D Biol Crystallogr **60:** 1214-1219.

ZHANG, M., T. TANAKA and M. IKURA, 1995 Calcium-induced conformational transition revealed by the solution structure of apo calmodulin. Nat Struct Biol 2: 758-767.